Electric-Field Affected Low-Energy Collisions between Co-Trapped Ammonia and Rubidium

by

L. Paul Parazzoli

B.S., University of Washington, 2001

A thesis submitted to the

Faculty of the Graduate School of the

University of Colorado in partial fulfillment

of the requirements for the degree of

Doctor of Philosophy

Department of Physics

2010

This thesis entitled:
Electric-Field Affected Low-Energy Collisions between Co-Trapped Ammonia and Rubidium
written by L. Paul Parazzoli
has been approved for the Department of Physics

Heather J. Lewandowski

Thomas Schibli

Date

The final copy of this thesis has been examined by the signatories, and we find that both the content and the form meet acceptable presentation standards of scholarly work in the above mentioned discipline.

Parazzoli, L. Paul (Ph.D., Physics)

Electric-Field Affected Low-Energy Collisions between Co-Trapped Ammonia and Rubidium

Thesis directed by Prof. Heather J. Lewandowski

This thesis describes the effect of an electric field on the interaction between rubidium and ammonia at 100 mK. The ability to study low energy interactions between molecules and atoms provides new tools to understand how the processes that govern these interactions work. For example, the use of external electric and magnetic fields provides tools to spatially orient molecules to show how this affects the dynamics of the interaction. The use of electric fields have been proposed to affect dipole-dipole interactions, however we have showed that the space-orienting effect of the field can have a significant effect even in the absence of dipole-dipole interaction. To measure this effect, we trap ammonia molecules in a single quantum state using an electrostatic trap. Rubidium atoms are trapped in a magnetic trap which is overlayed with the ammonia trap. The two samples then interact with minimal center of mass collision energy and we measure the elastic and inelastic cross sections by careful analysis of the ammonia trap-loss profile.

Dedication

For my parents, Silvana and Claudio Parazzoli and to my sister Susan “Cicia” Parazzoli.

Acknowledgements

First I would like to thank my advisor, Heather Lewandowski, whose support and expertise got me through graduate school. I am Heather's first graduate student, which means that we had a lab and an experiment to build up from scratch from the beginning. Heather and I worked side-by-side throughout much of the experiment, which can at times be straining on a student/advisor relationship. However in the end her expertise and problem-solving skills were invaluable to the success of this experiment. On a personal side, while she can push her graduate student to work hard, she is also very caring and understanding and is a great advisor.

I would also like to thank my fellow graduate student Noah Fitch, once for bringing his electronics expertise to the lab and also for his support throughout the experiment. He has now dismantled our atom-molecule collision apparatus and is in the process of building an improved version. I wish him the best of luck on his new experiment. Also I'd like to thank my former undergraduate students, Daniel Lobser and Carrie Weidner, for their enthusiasm and their many contributions to the lab.

Contents

Chapter

Tables

Table

Figures

Figure

Chapter 1

Introduction

1.1 Cold Molecules

The study of cold molecules has has lagged behind cold atoms by many years. This is not because of the lack of interest in cold molecules, but rather it is due to the difficulty in preparing them. The complex structure of molecules, including their rotational and vibrational levels make them difficult to cool using the traditional methods that have been so successful and producing ultracold atoms. Despite the difficulty, however, the field of cold molecules is becoming very promising as the techniques to prepare cold molecules continue develop and improve.

A lot of the motivation towards cold molecules is driven by the success of ultracold atoms. Ultracold atomic gases have contributed the discovery of new physics and have had many diverse applications including inertial sensing, the study of superfluidity, precision measurement of micro–scale forces, and new platforms for quantum computing. All of this success is only possible because of the level of control that can be wielded on the atoms only in the ultracold regime where they can be prepared in specific internal states and their external motions can be minimized. It is understandable from these achievements why it would be desirable to be able to impart that same level of control onto molecules with their rich internal structure.

The production of cold molecules will open up new avenues for studying interactions between molecules, precision measurement, dipole interactions for modeling quantum mechanical interactions in solids, and even quantum computing using dipolar molecules. In the area of low energy interactions, both scattering processes as well as chemical reactions can studied. Direct observation

of the complex processes that govern the interactions are difficult to make, however being able to control the interactions will elucidate some of these processes and help us better understand how the quantum mechanical nature of the interactions.

1.2 Measuring Cross Sections in Beams and Traps

Thus far, the use of molecular beams for scattering experiments has been widely implemented. The extremely high densities ($\mathcal{O}(10^{13})$ cm^{-3}) of these beams makes them well suited for measuring cross sections and product states, which can be done by crossing two beams with each other. The crossed molecular beam apparatus was originally demonstrated by Taylor and Datz in 1953. And in 1986 the Nobel Prize in Chemistry was awarded to Dudly Hershbach, Yuan T. Lee, and John C. Polanyi for their work involving the use of cross molecular beams [21]. Although a highly successful tool, one handicap of crossed-beam experiments is the lack of control one has over the beams. In molecular beams, one has limited control over the speed of the beam. And in addition, the quantum-state distribution of the beam is set by the temperature of the beam, which is roughly 3 K. The advent of Stark deceleration, however, has enabled unprecedented control over both the internal and external degrees of freedom of polar molecules in a beam. Stark deceleration is a state-selective method that allows one to precisely tune the velocity of the molecular beam over a wide range. As is discussed later, Stark deceleration gives the ability to study molecular scattering processes as a function of collision energy and with very high energy resolution [36, 16]. In addition to controlled cross-beam experiments, Stark deceleration also opens up the possibility of trapping neutral polar molecules that have been decelerated to sufficiently low velocities. These molecules can be trapped by a variety of methods such as electrostatic, magnetic, or AC traps and can be held for a duration of several seconds[1] . With cold trap temperatures around 10 to 100 mK, a homogeneous quantum state distribution, and the long interaction times, trapped samples are ideal for scattering and reaction studies.

There are several configurations for using a Stark decelerator for collision studies. The

[1] Typically limited by background gas collisions and possibly optical pumping from black-body radiation

simplest is to use it as part of crossed molecular beam apparatus [16] where the interaction energy can be tuned over a wide range and with an intrinsically high energy resolution. Alternatively, one can further reduce the collision energy by trapping one sample of molecules and use a continuous beam of another as a target [42, 41]. The hybrid-trap system also adds a level of flexibility as it allows for longer interaction time and therefore does not require a high density of the target beam. Both of these methods offer the ability to tune the interaction energy over a wide range allowing studies to probe resonances and explore details of the potential energy surface. A third method, described here, is to trap both samples in separate but overlayed traps. Having cotrapped samples takes away the ability to tune the interaction energy, however has the advantage that the interaction energy is dictated by the temperature of the trap and not limited by the center-of-mass velocity of the beam. In addition, because of the inherently low collision energy, elastic scattering events do not contribute to trap loss, consequently all trap losses are contributable to inelastic collisions. This is significant because in a beam-trap arrangement, the beam will typically have enough energy to kick the molecules out of the trap, therefore making it difficult to differentiate between elastic and inelastic collisions. Moreover, in a cotrap apparatus and under certain circumstances, the elastic cross section can also be extracted from the measurement of the trap-loss profile. This possibility is discussed later in this thesis.

1.3 Overview

In this work, we investigate the low energy (100 mK) interactions between ND_3 and Rb with the application of an electric field. We do this by trapping the ND_3 and the Rb in separate traps (magnetic for Rb and electro-static for ND_3) and then overlaying the traps so that the ND_3 and Rb interact. Our desire is to measure the scattering cross section between Rb and ND_3. Initially we attempted this measurement by passing a beam of ND_3, prepared in a specific quantum state, through the magnetically trapped Rb. Then by using a state-selective detection method we could measure the inelastic (i.e. state changing) collision rate. An important parameter in studying scattering events is the collision energy of the scatterers. Using a Stark decelerator gives us the

ability to control the velocity of the ND_3 as it passes through the Rb trap and thus control the collision energy. In this way, we could map out the dependency of the inelastic scattering cross section on the collision energy, exposing any resonance effects and the threshold behaviors of energy transfer in the rotational states of ammonia. After a great amount of effort, we determined that we did not have sufficient signal-to-noise to to measure the small cross-section between Rb and ND_3 . In order to measure a cross section of this size, we needed a longer interaction time between the Rb and ND_3 . While putting the ND_3 into a trap would take away our ability to control the collision energy, it would give us the necessary interaction time to measure the cross section.

Original calculations for the Rb-ND_3 system showed a very small cross section and did not agree with our measured results from our cotrap experiment. These calculations, however, were made for the case of no electric field. Because Rb has an extremely small dipole moment in our electric field, the dipole-dipole interaction is not significant and we did not expect the presence of the electric field, which is used for trapping the ND_3 , to have an effect on the collision rate. However closer look at the potential energy surface of the interaction reveals that Rb has a space-orientating effect on the ND_3 , i.e. the Rb causes the ND_3 to quantize along a space-fixed axis. In the absence of an electric field, ND_3 has to preferential spatial orientation and therefore, the Rb can easily project the ND_3 . This orienting effect is the origin of the small scattering cross section. When an electric field is applied however, then both the Rb and the electric field compete with each for the quantization of the ND_3 along different space-fixed axes. This competition dramatically affects the potential energy surface for the interaction and increases the inelastic cross section significantly. Experimentally we measure this increased cross section which results from the electric field. We measure the cross section using two isotopes of Rb and two isotopes of ND_3 for a total of four isotopic combinations,

$$^{14}ND_3 \rightarrow\leftarrow ^{87}Rb$$

$$^{15}ND_3 \rightarrow\leftarrow ^{87}Rb$$

$$^{14}ND_3 \rightarrow\leftarrow ^{85}Rb$$

$$^{15}ND_3 \rightarrow\leftarrow ^{85}Rb.$$

In addition, we also have the ability to vary the electric field slightly by decreasing or increasing the electrostatic trap strength. The Rb-ND_3 already sample various field strengths by nature of the electric field gradients in the trap, however by varying the trapping potential, we can effect the average field strength sampled during the interaction. The amount that we can vary the electric field is limited as going too low in field strength makes it difficult to trap the molecules and going too high can result in high voltage breakdown. We can however vary the trap strength by roughly 25% and we show that over this range, there is no appreciable effect to the collision cross section.

We use a novel analysis method involving the use of Monte-Carlo simulations to extract the inelastic cross sections while at the same time being able to place upper limits on the inelastic cross sections. This method takes advantage of the effect that elastic scattering of the ND_3 with the Rb in the trap causes the ND_3 to thermalize with the Rb. This thermalization affects the form of ND_3 trap loss profile, which is a measure of the ND_3 density at the center of the trap over time, and by measuring this effect, we can extract elastic cross section[2] .

[2] The precision that the elastic cross section can be measure with depends on the ratio between the elastic and inelastic cross sections (σ_e/σ_i). A larger ratio σ_e/σ_i results in a larger measurable effect and therefore leads to a more precise measurement. In the Rb-ND_3 system, σ_e/σ_i is only large enough to place upper limits on the elastic cross section

Chapter 2

The Apparatus

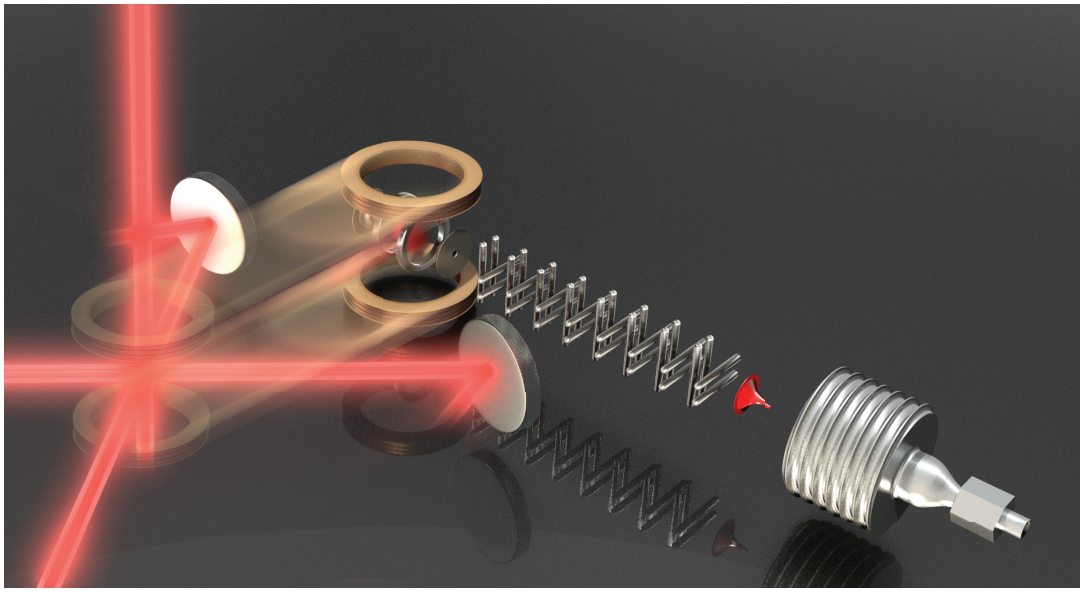

Figure 2.1:

The apparatus used in this work consists of two separate and independent apparatus that are combined to create a single experiment. One apparatus is used for cooling and trapping rubidium atoms. This apparatus produces a high number of cold rubidium atoms using a magneto-optical trap that are then transferred into a quadrupole magnetic trap. The second apparatus consists of a Stark decelerator, which is used to decelerate a cold molecular beam created from a supersonic expansion. After the molecular beam is slowed, it is loaded into an electrostatic trap. The rubidium trap and ND_3 trap are then combined and the interaction is studied by measuring the loss of the

ND_3 trap due to inelastic collisions with the rubidium.

2.1 Stark Deceleration for Controlling Molecular Beams

In the past decade, Stark deceleration has become a well established technique to decelerate and trap beams of neutral polar molecules. This technique utilizes time-varying, inhomogeneous electric fields to decelerate polar molecules and allows for precision control of the velocity of the molecules. The efficiency of the decelerator depends on how well the molecular beam is prepared before it enters the decelerator. Some important parameters include the density, velocity, velocity spread, and quantum state distribution, which are all set by the molecular beam source.

2.1.1 Molecular Beam Source

Cold molecular beams are used extensively in physical chemistry experiments and are created by a technique called supersonic expansion. In the process of supersonic expansion, a thermal reservoir of gas is separated by a small orifice from a region of significantly lower pressure. As the gas passes through the orifice from the high pressure (1 atm) to low pressure region, it undergoes collisions that act to cool the gas. In our case, a small percentage of ammonia is mixed with krypton as a buffer gas. After many collision with the krypton during the expansion, the ammonia molecules lose their rotational and vibrational energy and end up in the ground state. In addition, the expansion causes a redistribution of the velocities of the molecules in the gas corresponding to a temperature of $\sim 1\ K$. While the velocity distribution of the gas is much narrower, the translational energy of the gas is still very high–typically hundreds of meters per second. The speed of the molecular beam depends on the efficiency of the cooling of the gas during the supersonic expansion. Assuming that a significant amount of cooling occurs, i.e. most of the kinetic energy in the gas gets converter to the translational kinetic energy of the beam, then the maximum velocity of the beam is

$$v = \sqrt{\frac{2R}{m}\frac{\gamma}{\gamma - 1}(T - T_0)}, \tag{2.1}$$

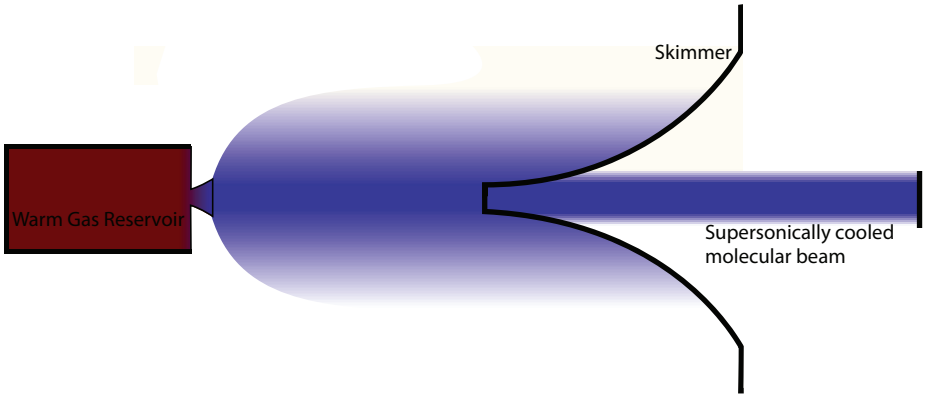

Figure 2.2: Schematic of a supersonic molecular beam.

where, m is the molecular mass and T_0 and T are the initial and final temperatures of the gas and $\gamma = 2.3$ for noble gases. The final velocity and temperature obtained by the molecular beam depend on "efficiency" of the expansion. From energy conservation requirements, the final temperature of the gas and the velocity of the beam are related by

$$Nk_{\mathrm{B}}T_0 = Nk_{\mathrm{B}}T + \frac{1}{2}Mv^2, \tag{2.2}$$

where N is the number of molecules and k_{b} is the Boltzmann constant. Therefore an optimal expansion (i.e. $T \approx 0$) leads to the greatest beam velocity given by Eqn. 2.1.

There are many different valve technologies for making molecular beams including RM Jordan Valves [25], solenoid driven general valves, and piezo-electric transducer (PZT) valves. Two important considerations in choosing an appropriate valve is the opening time of the valve, which determines how much gas enters the chamber, and also heating effects from the valve. The opening time is important for Stark deceleration because the limited spatial acceptance of the Stark decelerator only allows a small portion of the molecular beam to be decelerated. Therefore if the molecular beam is too long, only a small portion of the beam is decelerated. The rest of the gas only contributes to higher pressures in the chamber, which can result in a poorer supersonic expansion or reduce the lifetime of the trapped molecules. In addition, heating of the beam which may be caused by current-loop actuated valves such as the RM Jordan valve can lead to lower densities of

molecules being decelerated. Another important aspect is the stability of the valve.

Both shot noise as well as long term stability are dictated by the actual valve used to create the supersonic expansion. After some consideration, we decided to use a PZT valve modeled after the Proch-Trickl valve [39] shown in Figure 2.3. The advantage of this valve is its long term stability, reasonable shot to shot repeatability, and its relative simplicity means it can be constructed in-house at a low cost. The PZT valve uses a PI-286 high voltage PZT disc translator with a maximum displacement of 200 μm and can apply a maximum force of 5 lbs. The opening time of the valve is estimated to be around 100 to 200 μs. This opening time is likely limited by the dynamics of the rubber o-ring used to seal the orifice of the valve.

2.1.2 Stark Deceleration

Stark deceleration is one method for decelerating a cold but fast moving molecular beam. The principle operation of a Stark decelerator relies on the fact that a polar molecule placed in an electric field will experience a Stark shift of its internal states. The motion of the molecule can then be manipulated by using electric field gradients. In the high-field limit, the molecule will experience a force proportional to the electric field gradient by,

$$\vec{F} = -\vec{\mu} \cdot \nabla \vec{E}, \tag{2.3}$$

and in a direction (parallel or anti-parallel to the gradient) that is determined by whether the molecule is in a high-field seeking (HFS) or low-field seeking (LFS) state. While both HFS and LFS molecules have been decelerated [5], for this experiment, we work only with the LFS state of ammonia.

The Stark decelerator consists of a series of electrode pairs, where each pair of electrodes generates an electric field with a peak of about 10^5 V/cm directly between them. The basic operation of a Stark decelerator for LFS states is shown in Figure 2.4. Figure 2.4 shows two configurations for the application of the high voltage to the decelerator. As the LFS molecules approach the first pair of electrodes in configuration I (where the even electrode pairs are charged

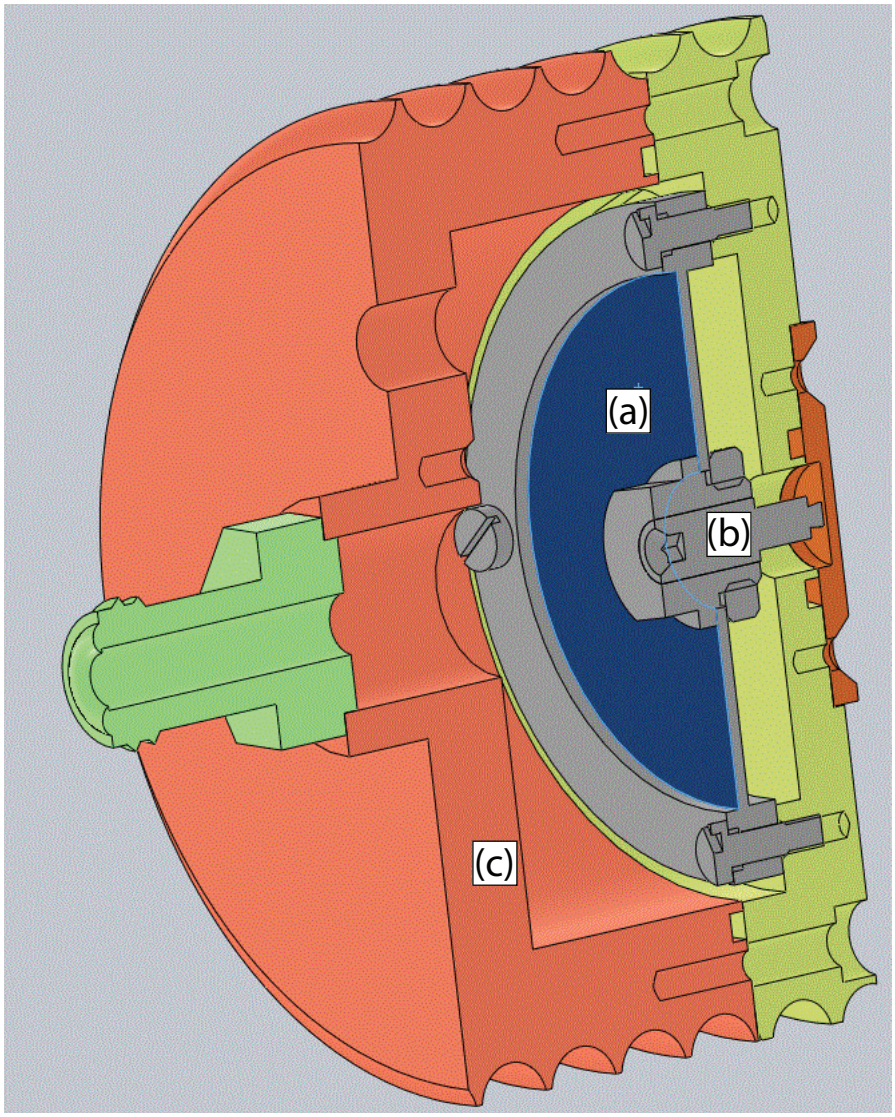

Figure 2.3: PZT valve as the molecular beam source. The valve uses a high-voltage PZT disc translator (a) to pull back a poppet (b) up to 200 μm creating a pulsed molecular beam of about 100-200 μseconds. The valve body (c) is constructed of stainless steel.

and the odd electrode pairs are grounded), they will experience a longitudinal force slowing them down as they approach the charged electrodes. If the decelerator is left in this configuration, the molecules will regain their lost kinetic energy after they pass the electrodes. So instead, the decelerator is switched to configuration II where the molecules will once again find themselves near the bottom of the potential and moving towards the next pair of charged electrodes. As this process is repeated, the molecules lose more and more of their kinetic energy with each stage of deceleration. For ammonia, with a typical dipole moment of about 1.5 debeye, and a feasible electric field of about 10^5 V/cm, a single electrode pair can remove about 1 cm[1] (or about 1%) of kinetic energy of the molecule. As such, over 100 electrode pairs must be used in series to decelerate the molecular beam. Our particular decelerator, (Figure 2.5) has 150 stages with an overall length of 0.81 m.

The output velocity of a Stark decelerator is tuned by specifying the precise position of the molecules within each stage for when the decelerator is switched from configuration I to configuration II. This then allows for precise control over how much energy is removed from the molecules at each stage of the decelerator. To determine the timing for switching the decelerator, a synchronous molecule is defined such that the decelerator is switched when the synchronous molecule is at a position defined by the phase angle $\phi_0 = \pi z/L$, where z is the position of the synchronous molecule within the stage and L is the length of a single stage. Non-synchronous molecules are also slowed, however, the amount of slowing that occurs is different from stage to stage, depending on their relative position to the synchronous molecule. The non-synchronous molecule may experience additional slowing while it is ahead of the synchronous molecule followed by less slowing when it falls behind the synchronous molecule. In this way, there is always a restoring force that confines the non-synchronous molecules around the synchronous molecule in a way that is analogous to the operation of a linear accelerator. The restoring force gives rise to ponderomotive potential, which acts to trap the molecules around the synchronous molecule with a phase space acceptance shown in Figure 2.6. The phase-space acceptance of the Stark decelerator defines the maximum distance and the maximum deviation in velocity (which of course are coupled to each other) a non-synchronous molecule can have and still be decelerated. The phase-space acceptance is determined

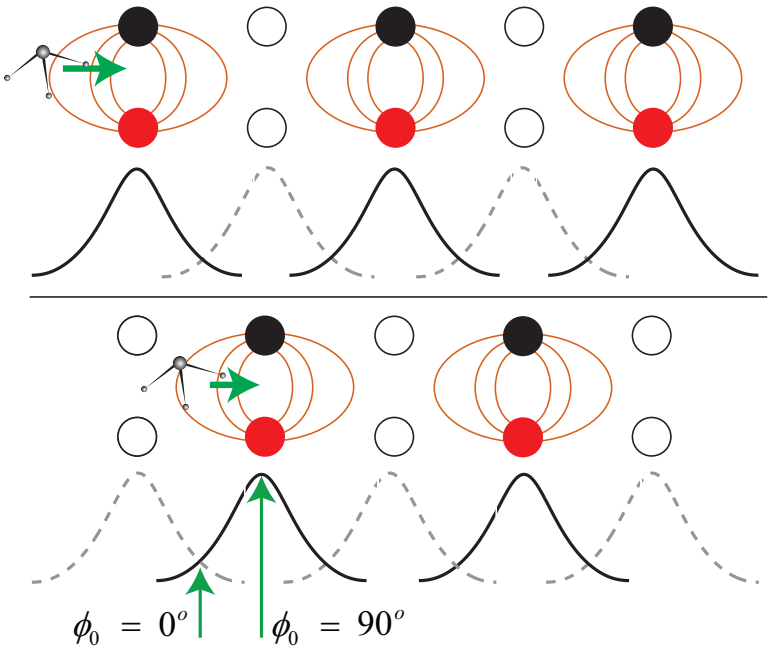

Figure 2.4: Operation of a Stark decelerator. As molecules enter, the decelerator is set to configuration I creating a large electric field gradient causing the molecules to lose kinetic energy as they approach the first pair of electrodes. Before the molecules reach the maximum of the electric field, the decelerator is switched to configuration II. This prevents the molecules from regaining its kinetic energy as they pass through the first stage. This process is repeated for 150 stages. The timing for which the decelerator is switched is determined by the position of a synchronous molecule such that the synchronous molecule is always at the same relative position within a stage when the fields are switched. The position of the synchronous molecule when the fields are switched is called the phase angle, $\phi_0 = \pi z/L$, where L is the length of a single stage and z is the position within a stage.

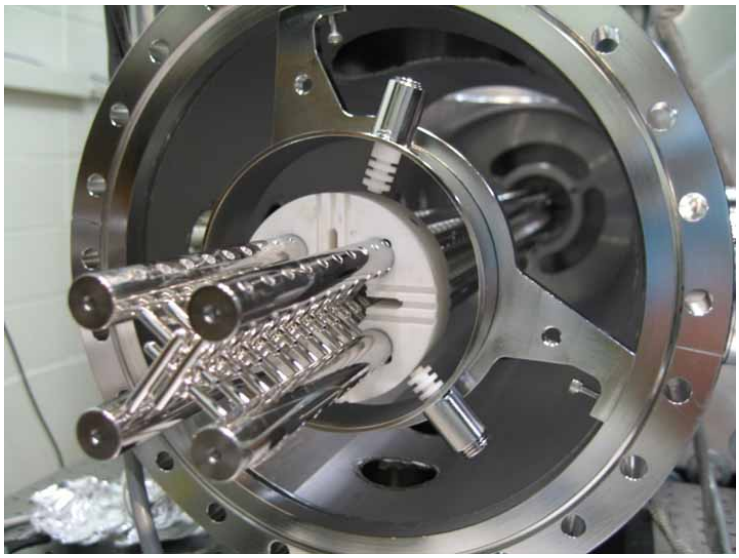

Figure 2.5: Photograph of the 150 stage Stark decelerator.

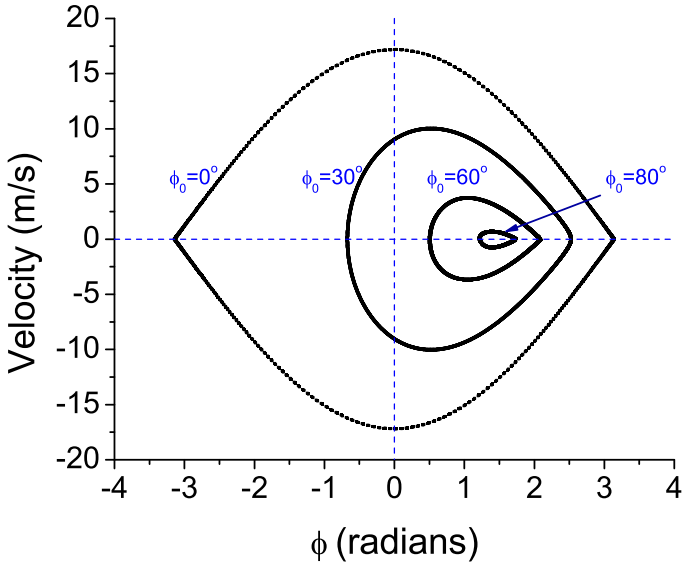

Figure 2.6: Phase-space trajectories for various slowing angles ϕ_0. The lines shown represent the orbits of the molecules at the boundary between between stable and unstable areas of phase space in the decelerator. For a given ϕ_0 the acceptance of the decelerator is the area within the boundary.

by the physical parameters of the Stark decelerator as well as the phase angle by,

$$\frac{\mathrm{d}^2\Delta\phi}{\mathrm{d}t^2} + \frac{W_{\max}}{mL^2}\frac{\mathrm{d}\Delta\phi}{t}\left[\sin(\Delta\phi + \phi_0 - \sin(\phi)\right] = 0, \tag{2.4}$$

Where $W_{\max}$ is the maximum amount of energy removed from the molecules by the slowing stage (i.e. at $\phi_0 = 90°$), m is the mass of the molecule, L is the length of a slowing stage, and $\Delta\phi$ is the offset in phase of the non-synchronous molecule from the synchronous molecule. As can be seen for the figure, more aggressive slowing comes with the trade-off that fewer molecules get decelerated overall. In order to trap the molecules, it is necessary to decelerate them to roughly 30 m/s, which corresponds to a phase angle $\phi_0 \approx 60°$.

2.2 Electrostatic Trapping

Stark decelerated molecules have been trapped by a variety of methods: electrostatically [15] [51]; magnetically [42], and in an AC trap for high-field seeking states [8]. In this experiment, we use an electrostatic trap to trap low-field the seeking state of ND_3 ($|JK\rangle = |11\rangle$).

2.2.1 Trap Loading

After the slowed ammonia exits the decelerator it is loaded into a quadrupole electrostatic trap which is shown if Figure 2.8. In its simplest form, a quadrupole electrostatic trap could be designed with three electrodes [15], where the center two electrodes in our design would be single electrode. However there are two major advantages in the four-electrode design: (1) it gives access for the rubidium to be transferred to the center of the trap; and (2) it has greater versatility in creating various electric field configurations to efficiently load the trap. These potentials for the trap loading configurations, shown in figure 2.10, create potential hills to remove energy from the molecules as they enter the trap. The intent of this sequence is to minimize the temperature of the trap by bringing the molecules to rest as close to the center of the trap as possible.

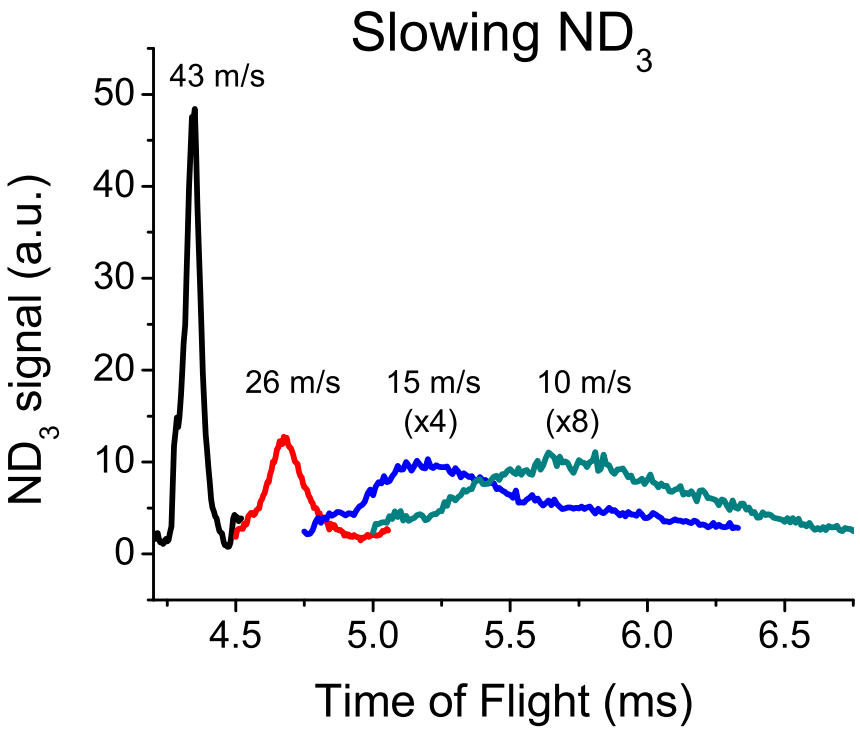

Figure 2.7: Slowing ND_3 to various velocities. The time of flight traces of ND_3 is plotted. It is clear that number of phase-stable molecules decreases as the slowing angle increases and the molecules are more aggressively slowed.

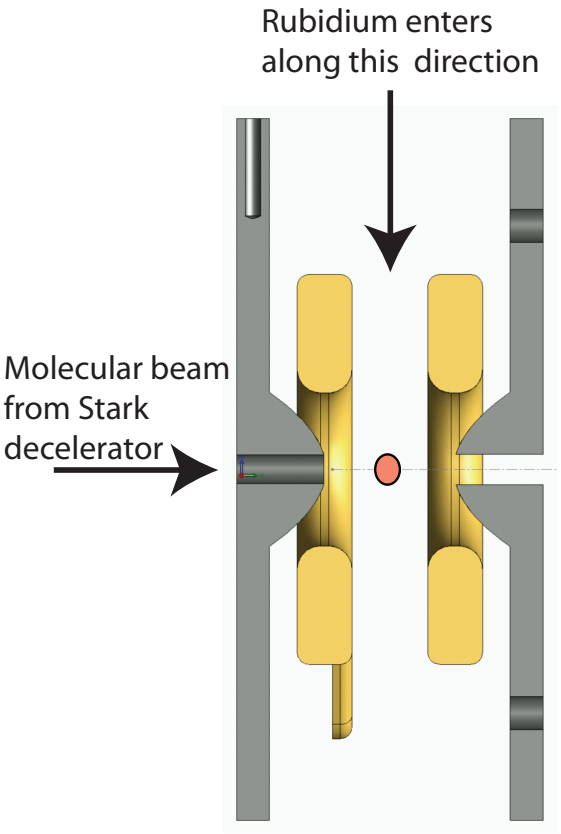

Figure 2.8: Diagram of the quadrupole electrostatic trap. Having two split rings in the center, as opposed to a single ring allows us to bring the Rb trap in from the side. In addition being able to have different charged electrode configurations allows us to move the longitudinal trap center, which makes it easier to load the trap.

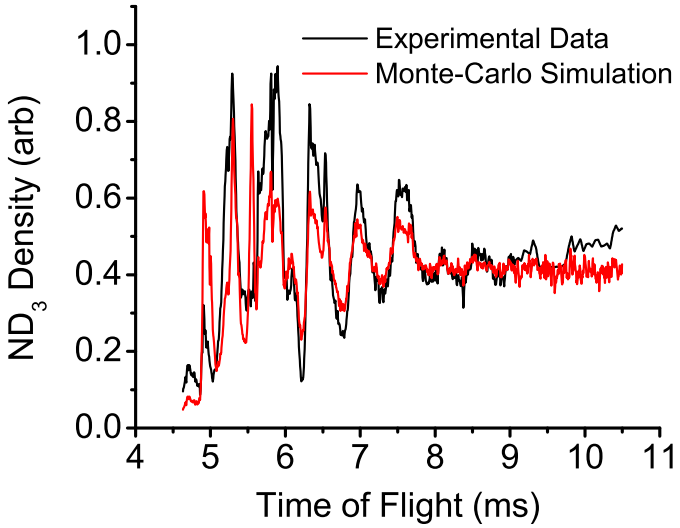

Figure 2.9: Loading of the electrostatic trap. The black trace shows ND_3 density at the center of the trap is shown as a function of time since the opening of the valve. The results of Monte-Carlo simulations recreating the trap loading sequence is shown in by the red curve. The turn-on time for the trap in this case is at 5.4 ms. After the trap is turned on, there are several oscillations in the density at the center as the ammonia cloud slosh backa nd forth in the trap. These oscillations dampen down after a few milliseconds.

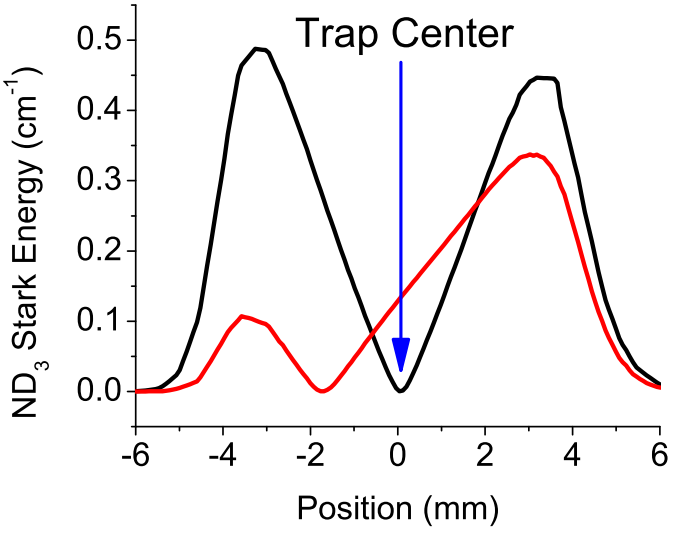

Figure 2.10: Longitudinal slowing potentials generated by applying high voltage to different combinations of trap electrodes. Being able to bring the molecules to a stop near the center of the trap is important in minimizing the temperature of the trap.

2.2.2 Optimization of Trap Load

As mentioned earlier, the number of molecules captured in the trap as well as the temperature depend critically on the loading parameters of the trap and particularly the speed of the molecules as they enter the trap. To minimize the temperature of the trap, it is necessary to bring the molecules to rest at the center of the trap. This would result in a temperature of approximately 35 mK[1] . To stop the molecules at the center of the trap, however, would require the molecules to be decelerated to such a low velocity (roughly 24 m/s) that the packet would spread out significantly before entering the trap resulting in only a small fraction that could be confined. At the other extreme, if the molecules enter at too high of a speed, many of the molecules will fly over the trap walls and the remaining molecules will enter with significant kinetic energy, resulting in a higher trap temperature. For our particular purpose, collecting a large number of molecules in the trap is important to be able to accurately measure the 1/e lifetime of the ND_3 . The actual temperature thus is less important. We therefore tune the trap loading parameters to maximize the number of molecules in the trap.

Optimizing the trap loading parameters can be an arduous task. Specifically the one-dimensional trajectory calculations that are used to determine the timing for switching the decelerator become less suitable at low velocities where the transverse motion of the molecules begins to to have a significant effect. As the molecules enter the trap there is significant coupling between the longitudinal slowing of the molecules and the transverse confinement. Add to that, the need to optimize the speed of the molecules entering the trap and it becomes an issue of optimizing for a large and complicated parameter space. To ease the task of optimizing the decelerator loading, we employ an evolutionary-algorithm based optimization tool. This method boasts an 80% increase in ND_3 trap density in a single day over a week's worth of manual optimization based on trajectory simulations [2] .

[1] This temperature is estimated based on the mean speed of the molecules in the moving beam frame using the formula $T = mv^2/(3k)$. The actual distribution of the molecules, however, is non-thermal and is determined by the phase-space acceptance of the decelerator and the trap. Therefore this temperature measurement is only an approximation.

[2] Special thanks to Dan Lobser for convincing me it was worthwhile to try.

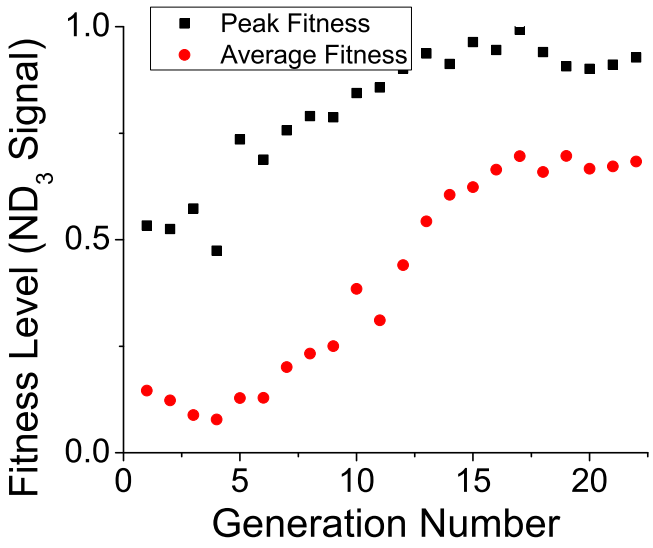

Figure 2.11: Optimization of the trap loading sequence using a genetic algorithm approach.

There are several implementations of evolutionary algorithms. The implementation we use is called an *evolutionary strategy* (ES) [14] where the solution to the problem (i.e. the optimal trap load) is encoded in a vector of real numbers. This vector of numbers, called the *genotype* sets the time, (t_i), for the various stages of trap loading and also for the final three decelerator stages, which sets the final velocity of the molecules. Changing the time, t_n, of a particular stage directly effects the timing of the subsequent stages $t_{i>n}$. Therefore, faster convergence is obtained by encoding the time sequence as a series of time-differences Δt_i, where $\Delta t_i = t_i - t_{i-1}$. The genotype consists of total of seven Δt_i parameters. The ES consisted of a population of 70 members where the fitness of each member is determined by the density of trapped ND_3 after 50 ms in the electrostatic trap. The crossover and mutation rates were empirically determined to be optimal at approximately 0.6 and .05 respectively. The overall efficiency of the algorithm could be increased by incorporating the crossover and mutation rates into the genotype, as is popularly done. Two methods were developed for splicing the genes from the parents to create offspring. In the *direct* method, the selected genes $(\Delta t_i's)$ from one parent were directly spliced into another parent to create the offspring. Alternatively, the *averaging* method, took the weighted average of the selected gene from each of the two parents, based on the relative fitness of the parents. The resultant gene was then spliced into a parent to generate the offspring. Though there is no precedence for the averaging method[3] , I thought it might be a clever approach. Unfortunately the averaging method was much slower to converge and did not produce better results.

Another parameter to consider in ES methods is the mutation width. In the beginning the mutation width should be large enough to cover a wide range of the parameter space, however as the solution converges, it is more efficient to have a small mutation width. However, in systems that have inherent noise associated with the measurement, it is important that the mutation width is always greater than statistical width of the measurement.

[3] At least to my knowledge

2.3 Rubidium Trapping

The rubidium is prepared basically in three steps: first, the rubidium is laser cooled and confined in a magneto-optical trap (MOT); following the MOT stage, the rubidium is then loaded into a magnetic trap; and finally, the magnetically trapped rubidium is physically transferred to the ND_3 trap region where the two samples are allowed to interact.

MOTs have become the workhorse of the atomic physics community. By applying appropriately polarized lasers and inhomogeneous magnetic fields, MOTs create a position-dependent force on the atoms as they scatter the light from the lasers. Comprehensive overviews of laser cooling techniques can be found in many sources [54, 55, 33]. Our MOT setup is shown if Figure 2.12. The MOT is prepared in a glass cell where rubidium vapor is provided via dispensers that release rubidium when heated. The reason for preparing the Rb in a separate chamber from the ND_3 is mainly because of the need for optical access for the MOT lasers, but also to maintain an high-vacuum region where the rubidium and ND_3 interact. The vacuum constraint is important as independent lifetimes of the rubidium and ND_3 are limited by background gas collisions.

The MOT beams come from Vortex diode lasers that are frequency stabilized using the D2 ($5^2S_{1/2} \longrightarrow 5^2P_{3/2}$) transition of the rubidium. Ideally, we would like to collect as many rubidium atoms as possible. We therefore used relatively large MOT beams. The MOT beams are magnified by a 7× telescope to around 5 cm with a maximum possible intensity of around 8 mW/cm^2 in each of the six beams. To obtain this intensity, a two-stage amplification system is employed. The first amplification is through a home-built slave diode laser which is seeded by the Vortex laser. This provides roughly 13 mW of injection power into a commercial tapered amplifier. The tapered amplifier can provide up to 500 mW of laser light. For the MOT however, we found that the optimal laser power is 354 mW and 254 mW for ^{87}Rb and ^{85}Rb) respectively, corresponding to intensities at the MOT cell of roughly 5.6 mW/cm^2 and 4 mW/cm^2 in each beam respectively.

Following the MOT stage, the rubidium is spin polarized and transferred into a quadrupole magnetic trap. The rubidium is trapped in its stretch state ($F = 2, m_f = 2$ for ^{87}Rb and $F =$

$3, m_f = 3$ for ^{85}Rb), where it is most tightly confined. The magnetic trap is provided by a pair of electromagnetic coils, roughly 10 cm in diameter, each with 24 turns and 500 amps of current. The magnetic coils provide an axial field gradient of 300 Gauss/cm (half that in the radial dimension). We obtain magnetic trap densities of 1.1×10^{10} atoms/cm^3 for ^{87}Rb and 3×10^9 for ^{85}Rb with temperatures close to 600 μK.

Once the magnetic trap is loaded, the rubidium must be overlayed with the electrostatic ND_3 trap. This is accomplished by physically moving the magnetic coils 50 cm along a linear translation stage. The linear stage is controlled by a servo with a reproducibility of 5 μm. Proper alignment of the rubidium trap with the ND_3 trap is crucial. Figure 2.13 shows a schematic of the alignment dimensions and their labels. Alignment in the vertical dimension as well as the dimension along the horizontal linear stage axis are done using ion detection of the rubidium. We non-resonantly ionize the rubidium using a focused UV laser at around 317 nm. Along the vertical axis the laser is scan vertically to ensure the center of the rubidium cloud overlays with the center of the ND_3 cloud which, is measured in the same manner. Along the linear stage axis, the alignment is slightly more difficult. We cannot scan the laser in this dimension, so instead the rubidium trap width is convolved with the 2 mm vertical exit slit of the electrostatic trap[4] . The ion detection efficiency falls off away from the center of the slit and therefore the convolution of the rubidium cloud with the horizontal detection efficiency will have a maximum when the center of the rubidium cloud is aligned with the center of the exit slit. Finally, along the horizontal axis of the Stark decelerator, the alignment of the rubidium becomes especially tricky. Along this dimension, we measure the lifetime of the rubidium, as it is overlayed with the electrostatic trap, as a function of its horizontal position. As discussed later, the strong electric fields created by the electrostatic trap, Stark shifts the rubidium, causing them to fall out of the trap. Therefore, at the center of the electrostatic trap, where the electric field is a minimum, the rubidium trap has the longest lifetime. This is a fairly accurate method (to within approximately 50 μm) for aligning the rubidium along the dimension of the Stark slower, however it is extremely tedious as it requires unbolting the linear stage and

[4] the exit hole is where the ions are extracted from within the electrostatic trap to the micro-channel plate detector

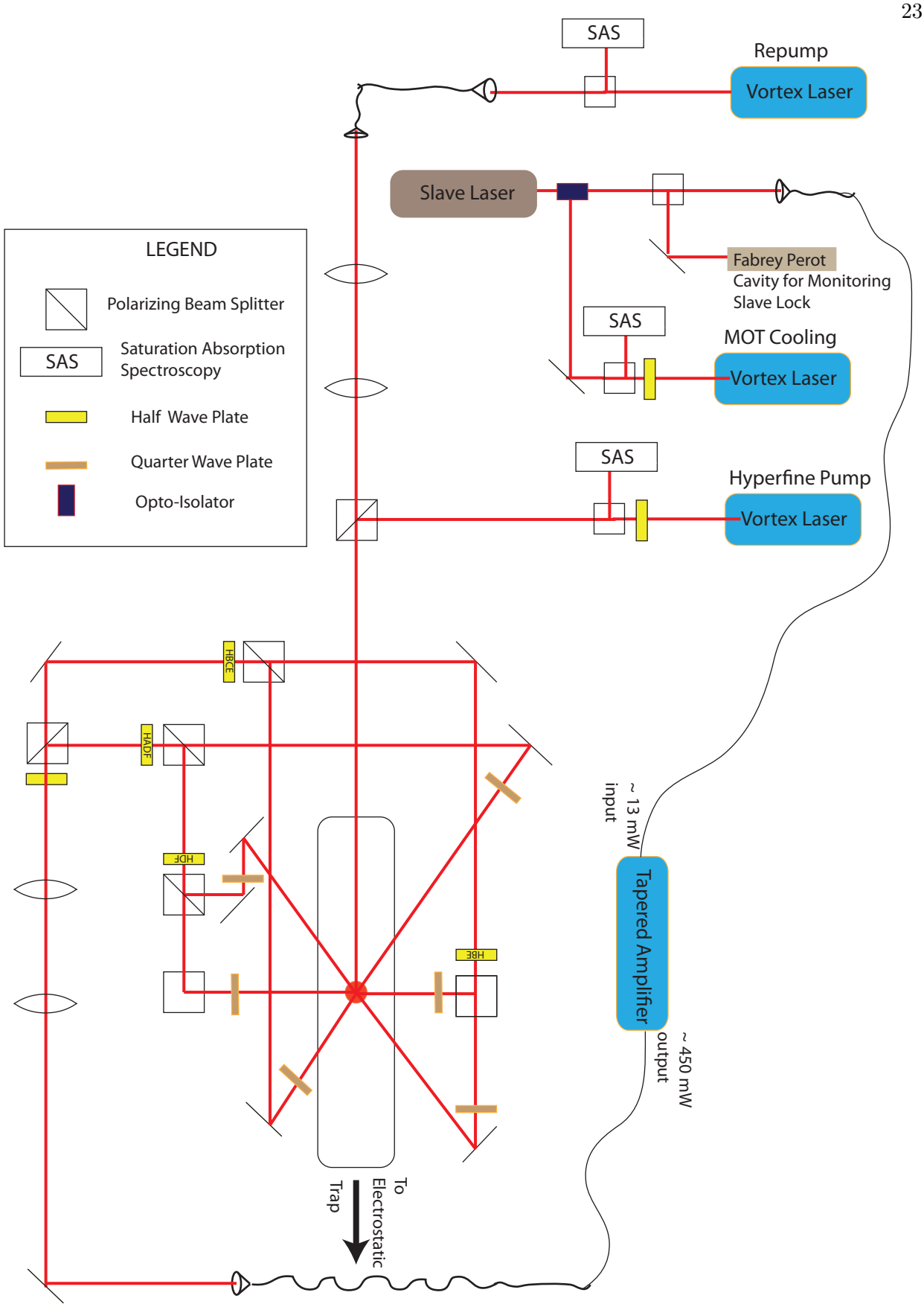

Figure 2.12: Rb trapping setup. Five cm trapping beams with and intensity of approximately 8 mW/cm^2 are used to cool and trap ^{87}Rb and ^{85}Rb atoms. Once loaded into a magnetic trap from the MOT stage, the atoms have a density of approximately 1.1×10^8cm^{-3} and a temperature of approximately 600 μK.

then carefully and precisely moving the track. The alignment of the rubidium trap in the vertical dimension as well as the linear stage dimension has a typical uncertainty of approximately 80 μm.

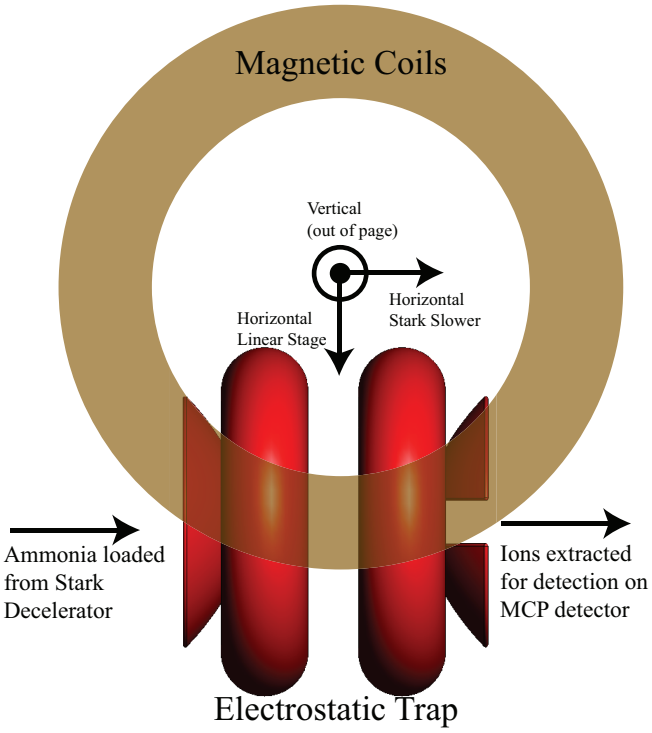

Figure 2.13: Schematic of the dimensions for aligning the rubidium trap with the electrostatic trap. In the vertical and horizontal linear stage dimensions, the rubidium is aligned with the electrostatic trap by ion detection. In the horizontal Stark decelerator dimension the rubidium is aligned by measuring the rubidium lifetime vs the position in the electrostatic trap.

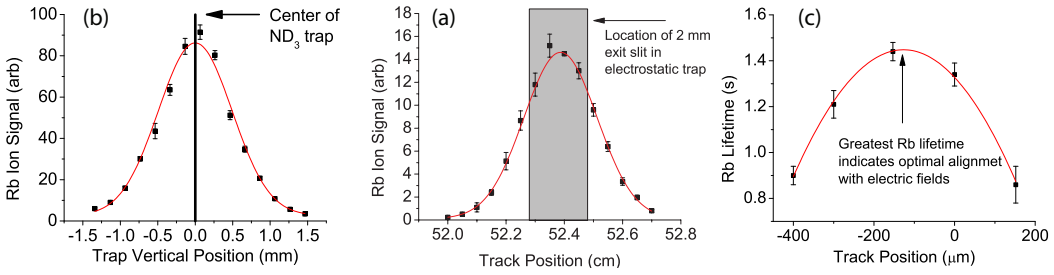

Figure 2.14: Aligning the Rb trap in the vertical (a), horizontal linear stage (b), and horizontal Stark slower (c) dimensions.

Chapter 3

Ammonia Molecule

3.1 Introduction

The ammonia molecule has had a rich and diverse history, especially in the 20^{th} century. Ammonia was a principle agent in the production of munitions during both world wars. It is also a key ingredient in fertilizers. In fact ammonia is so important to the world's agricultural industry that the 1918 Nobel prize in chemistry was awarded to Fritz Haber, who in collaboration with Carl Bosch developed a technique to produce ammonia on an industrial scale [53]. Ammonia is now also used as a refrigerant, in the manufacturing of materials such as nylon and plastics, and also in the production of pharmaceutical products.

Apart from its industrial applications, ammonia has also become an important molecule for science and in particular for astrophysical measurements. The inversion splitting of rotational level of ammonia are similar in energies. Therefore each rotational level can be observed using the same radiotelescope array, making it a good candidate for probing temperatures in interstellar space [32]. Also ammonia is abundant in interstellar clouds and many of the spectral lines observed in these clouds have been attributed to collisions of ammonia within these clouds. [37].

3.2 Ammonia as a Symmetric Top Molecule

Ammonia is an example of a symmetric top molecule. Generally, polyatomic molecules are described by their symmetry properties and are labeled according to their point group. A good introduction to symmetry properties and point groups is given by Herzberg [20]. Symmetric top

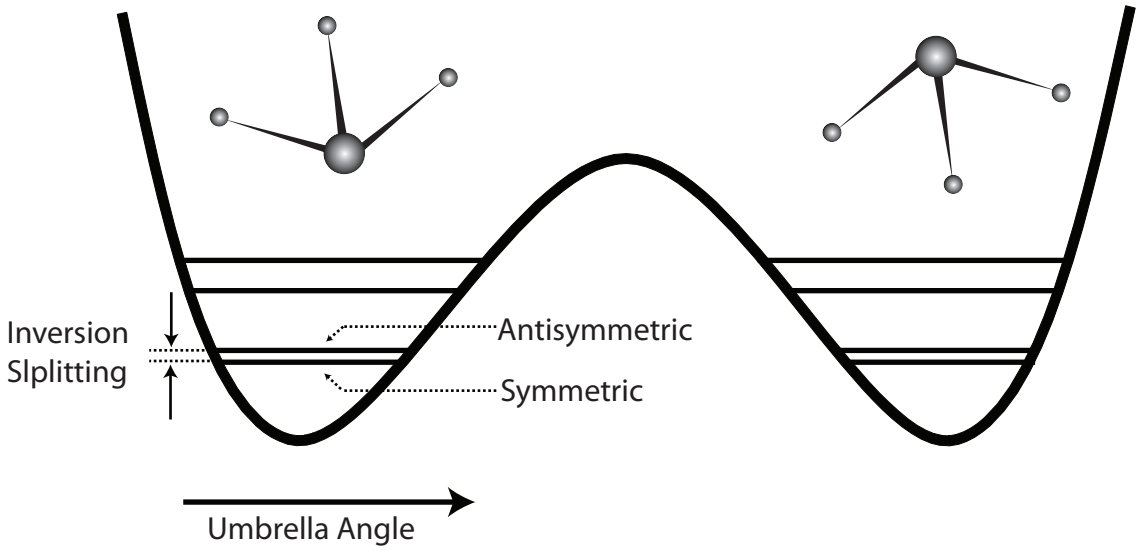

Figure 3.1: The potential energy of ammonia as a function of the umbrella angle. The umbrella angle is defined as the angle between the N-H (or N-D) bond and the symmetry axis of the ammonia. The two minimums of the double-well potential, corresponding to the *umbrella modes*, are at 68° and 112°. The potential barrier separating the two umbrella modes is approximately 2023 cm^{-1} and corresponds to the barrier preventing the nitrogen from tunneling through the plane of the hydrogen atoms. The inversion splitting shown is a splitting of all the rotational levels as a result of this barrier.

molecules can be labeled as having either C_{px} or D_{px} symmetry[1] . Where C_p symmetry indicates that it has a single axis with p-fold symmetry and no other symmetries. A molecule with D_p symmetry has, in addition to C_p symmetry, p two-fold symmetry axis which are perpendicular to the C_p axis and are separated by equal angles to each other. The x label indicates if it has p planes of symmetry only through the symmetry axis ($x = v$) or if it additionally has a perpendicular symmetry plane ($x = h$). The C_{3v} and D_{3h} point groups are illustrated in Figure 3.2 for an XY_3 molecule such as ammonia.

In its ground state, ammonia has a trigonal pyramidal structure with one nitrogen atom and three hydrogen atoms. Because of its pyramidal structure, ammonia only supports C_{pv} type symmetry and because it has 3 hydrogen atoms, $p = 3$ and is therefore labeled C_{3v}. In higher rovibrational states however, ammonia becomes planar and can be labeled D_{3h}.

The rotational energy levels of a symmetric top molecule is given by

$$F_{[v]}(J,K) = B_{[v]}J(J+1) + (A_{[v]} - B_{[v]})K^2 \pm 2A_{[v]}\xi K, \tag{3.1}$$

where J and K are the rotational quantum numbers for the total angular momentum and its projection onto the C_3 axis respectively. The last term on the right hand side is the coriolis term. The sign of the coriolis term is set by whether the vibrational angular moment is in the same direction (-) or opposite (+) of the rotational angular momentum. The constants $A_{[v]}$ and $B_{[v]}$ are the average values of rotational constants, $A_e = h/8\pi^2 cI_{A^e}$ and $B_e = h/8\pi^2 cI_{B^e}$. For a given vibrational level $A_{[v]}$ and $B_{[v]}$ are given by

$$\begin{aligned} B_{[v]} &= B_e - \sum \alpha_i^B \left(v_i + d_i/2\right) \\ A_{[v]} &= A_e - \sum \alpha_i^A \left(v_i + d_i/2\right), \end{aligned} \tag{3.2}$$

where d_i is the degeneracy of the vibration v_i. The constants α_i^A and α_i^B are related to the coupling between the rotational and vibrational states of the the molecule. And in the case of molecules with pyramidal structure (such as ammonia), where there is a possibility to invert the molecule (i.e. the

[1] Actually for symmetric top molecules, if it has D_p symmetry, then the molecule must be planar. Therefor, for symmetric top molecules $D_{px} = D_{ph}$.

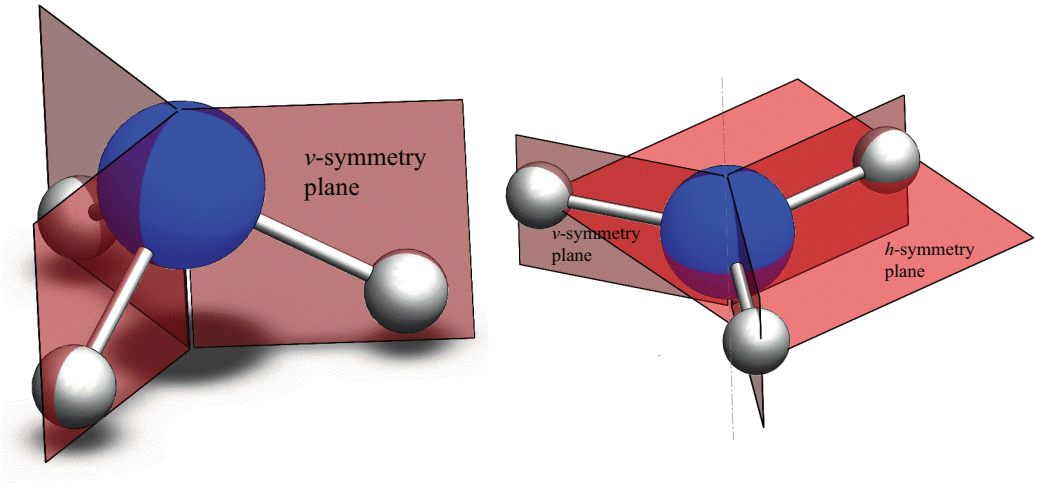

Figure 3.2: C_{3v} (left) and C_{3v} symmetries. Molecules with C_{3v} symmetry (such as the grounds state of ammonia) exhibit a splitting of their rotational levels into opposite parity states. This splitting, which is a result of the potential barrier which prevents the molecule from inverting itself, gives rise to the Stark shift.

nitrogen passing through the plane of the hydrogen atoms in the case of ammonia) the α_i constants cause a splitting of each of the rotational energy levels. The rotational levels are split into states of opposite parity, which gives rise to the Stark shift as the electric field causes the opposite parity state to repel.

3.3 Stark Shift in Ammonia

The ammonia molecule has a trigonal pyramidal structure with one nitrogen atom and three hydrogen atoms (or deuterium atoms for deuterated ammonia). The angle between the symmetry axis and the nitrogen-hydrogen bond is called the umbrella angle, ρ. There are two potential energy minimums for ρ, at 68° and 112°. Each of these points corresponds to a mode in which the nitrogen is either above or below the plane of the hydrogen atoms. These two modes are separated by a finite potential barrier (shown in Figure 3.1) through which, the nitrogen can tunnel. This tunneling potential gives rise to a doubling of each of the rotational levels into symmetric and antisymmetric states[2] known as the inversion splitting.

In addition to the J and K quantum numbers, when an electric field is applied, there is an additional quantum number, labeled M, which defines the projection of J onto the field axis. The Stark shift of the ammonia due to the electric field can be expressed as

$$W_{\text{Stark}} = \frac{W_{\text{inv}}}{2} \pm \sqrt{\left(\frac{W_{\text{inv}}}{2}\right)^2 + \left(\mu|E|\frac{\text{MK}}{\text{J(J+1)}}\right)^2}, \tag{3.3}$$

where μ is the electric dipole moment, $|E|$ is the magnitude of the electric field and W_{inv} is the inversion splitting, given as,

$$W_{\text{inv}}^{\text{NH}_3} = 0.79 \text{ cm}^{-1} \tag{3.4}$$

$$W_{\text{inv}}^{\text{ND}_3} = 0.053 \text{ cm}^{-1}. \tag{3.5}$$

[2] Only rotational levels that are below the tunneling barrier experience this doubling effect.

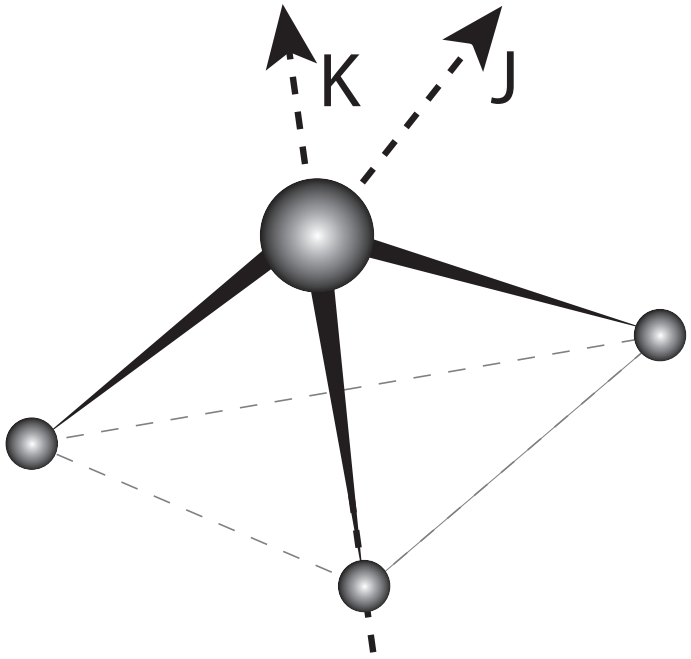

Figure 3.3: The ammonia molecule.

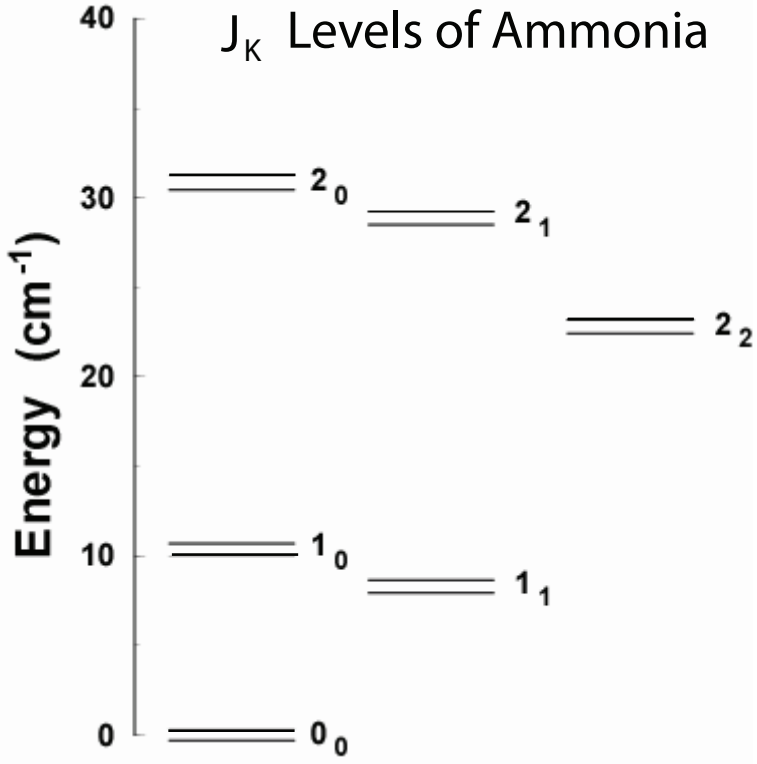

Figure 3.4: The J_K rotational states of ND_3 .

The $\pm$ in Eqn. 3.3 indicates the difference between the symmetric and antisymmetric states. For $MK \neq 0$, the electric field causes the two opposite parity states to repel each other, as shown in Figure 3.5 for the J=1 state. The low-field seeking states are the antisymmetric states and have Stark energies that increase with electric field strength. These are the molecules that are decelerated in the Stark decelerator. High-field seeking molecules cannot be decelerated by the conventional Stark decelerator as the maximum electric field strengths are at the electrodes and therefore the transverse stability of the molecules becomes an issue. Deceleration of high-field seeking molecules, however, has been demonstrated using and alternate gradient technique [5, 4]. The alternate gradient technique employs a series of electric quadrupole lenses that focus the molecules in one direction while defocusing them in the other direction. By alternating the orientation of these lenses, it is possible to obtain net focusing in both direction.

Figure 3.5, the Stark shifts for both ND_3 and NH_3 are shown in a characteristic electric field strength of a Stark decelerator. For the case of NH_3 the Stark shift remains quadratic throughout much of the decelerator. ND_3 however, because of its heavier deuterium atoms, has a significantly smaller inversion splitting and thus the Stark shift becomes linear at much smaller electric fields. This makes ND_3 a better candidate for Stark deceleration over NH_3, as the force exerted on the molecule, given by $F = -\mathrm{d}W/\mathrm{d}z$, is maximum in the linear regime of the Stark shift.

3.4 Detection of Ammonia

Detection of the ammonia is made by ionizing the ammonia and then, using an electric field, accelerate the ion onto a micro-channel plate (MCP) detector. The MCP consists of a low work-function metal which upon being struck by an ion emits a cascade of electrons that can then be read out on a scope via a transimpendence amplifier.

The ionization energy of ammonia is around 10 eV [30], so direct ionization using a single photon is difficult. Instead, to ionize the ammonia, we use a method called *resonance enhanced multi-photon ionization* (REMPI). REMPI is a state-selective non-linear optical process that is often used as a spectroscopic tool for studying molecular structure and decay dynamics of highly

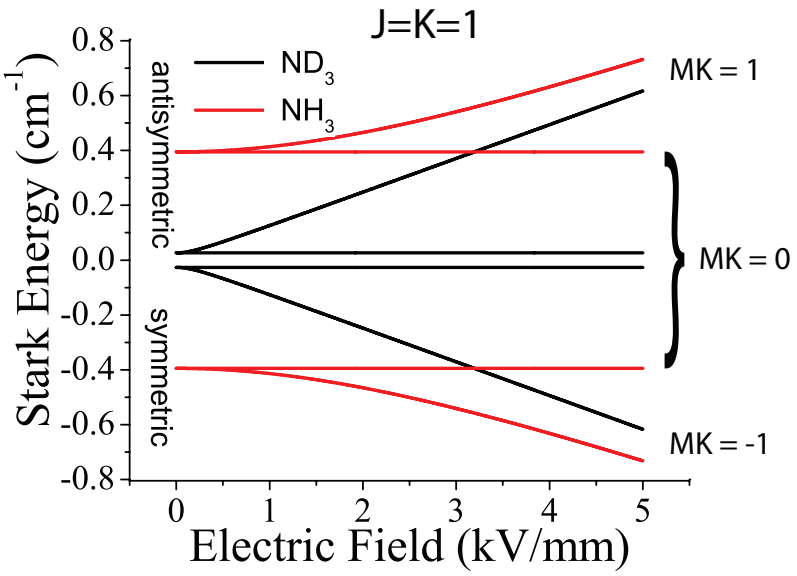

Figure 3.5: The Stark shift of ND_3 and NH_3. The force experienced by a polar molecule in the Stark decelerator depends on the spatial derivative of its Stark shift. The Stark shift for ND_3 becomes linear at very low electric field values as opposed to the Stark shift of NH_3 which does not become linear until nearly 3 kV/mm. For this reason, it is much easier to decelerate ND_3 .

excited electronic states [1, 2]. For detection however, REMPI is a convenient method of ionizing the ammonia using multiple photons that are within an energy range obtainable using dye lasers. Our particular ionization process is a 2+1 REMPI in which two resonant photons excite the ammonia to the Rydberg levels via the $\widetilde{B}(v_2 = 5) - \widetilde{X}(v_2 = 0)$. A third non-resonant photon then ionizes the ammonia. The ionization spectra of the upper inversion component of ND_3 is shown in Figure 3.6. The actual transition used in the experiment to detect the $|\mathrm{JK}\rangle = |11\rangle$ state is marked with a green arrow.

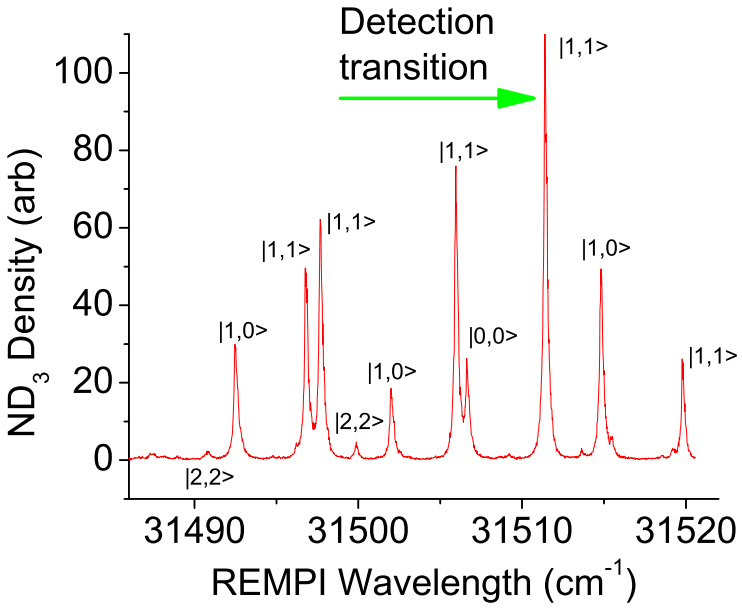

Figure 3.6: REMPI Spectroscopy of $^{15}ND_3$. The $—JK\rangle$ state the the ND_3 originates from is labeled. The transition used for detection is marked with a green arrow.

Chapter 4

Measuring the Rb-ND_3 Interaction

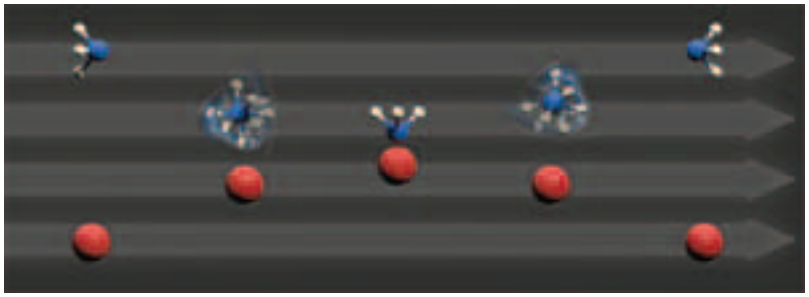

Figure 4.1: Artists rendition of Rb-ND_3 interaction. At large separation, the electric field (horizontal grey arrows) project the ND_3 along the field axis. At short range, the Rb projects the ND_3 along the interaction axis. At intermediate distances, the Rb and electric field compete with each other, causing the ND_3 state to become ill-defined, thus increases the probability for the ND_3 to change state.

4.1 The Rb-ND_3 Interaction

The large anisotropy of molecule-molecule interactions generally leads to large inelastic scattering cross sections, as it is not constrained by angular momentum conservation (such as the case for atom-atom interactions) [26]. The Rb-ND_3 system in particular has a highly anisotropic potential energy surface 4.3 As a general rule, inelastic scattering cross sections for highly anisotropic systems can be approximated by the Langevin capture formula [29] which states that if the interaction energy exceeds the centrifugal barrier, whose height is set by C_6/R^6, then there is unit

probability of an inelastic scattering event occurring. The cross section for this model is given by,

$$\sigma_{\text{Langevin}} \approx 3\pi \left(\frac{C_6}{4E_{\text{col}}} \right)^{1/3} \tag{4.1}$$

where E_{col} is the collision energy. Using the Langevin approximation and a C_6 of 4700 [23] we would expect a rather large inelastic cross section for the Rb-ND_3 interaction of $\sigma_{\text{Langevin}} \approx 4000$ Å^2. Calculations by $\dot{Z}$uchowski, et. al. however, show that the cross section for this system is surprisingly small [24], nearly a full order of magnitude smaller than predicted by the Langevin capture model.

Figure 4.2 shows the results of the calculations as well as the semiclassical approximation for the elastic cross section and the Langevin capture model. The results for the elastic cross section follow the semiclassical model quite closely. However the actual inelastic cross section deviates quite significantly from the Langevin model. This suppression in the cross section is surprising, however it can be explained as a result of the deep potential energy minimum shown in the calculated potential energy surface of the system in Figure 4.3. Far away from the Rb, the ND_3 is in one of its symmetric or antisymmetric eigenstates, labeled $|11u\rangle$ and $|11l\rangle$, which are linear superpositions of the ND_3 umbrella modes. However as the ND_3 approaches the Rb, the deep minimum in the potential energy surface causes the ND_3 to project along its C_3 axis (i.e. into one of its umbrella modes). The only energetically allowed inelastic channel is through the inversion splitting (i.e. $u \rightarrow l$ or $l \rightarrow u$), however these parity states remain well separated in energy throughout the interaction and therefore the likelihood of a transition between them is quite low.

Not included in this calculation is the effect of an electric field. As described in § 2.2, the ND_3 is trapped in an electrostatic trap. So as we are measuring the cross-section for the Rb-ND_3 system, we were initially surprised to discover that our empirically determined cross section do not agree with the calculations presented by $\dot{Z}$uchowski, et. al. Indeed, our measured results, detailed later, are significantly greater than expected, yet still not as large as the prediction based on the Langevin capture model. The explanation for this is in effect of the electric field on the ND_3 molecule. As explained earlier, the Rb atom acts to project the ND_3 molecule along a space-fixed axis as they approach each other. However, the electric field also projects the ND_3 along a different

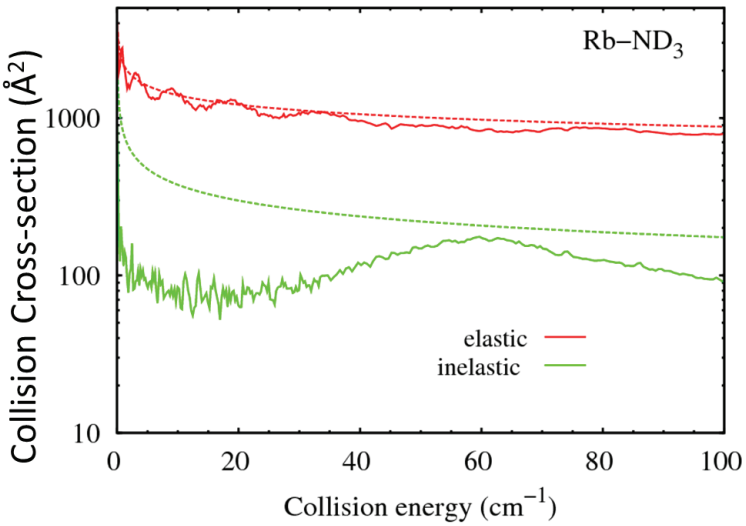

Figure 4.2: Elastic and inelastic cross sections for Rb-ND_3 scattering from Żuchowski et. al. [24]. The dash lines show the results of the semiclassical approximation for the elastic cross section and of the Langevin capture model for the inelastic cross section.

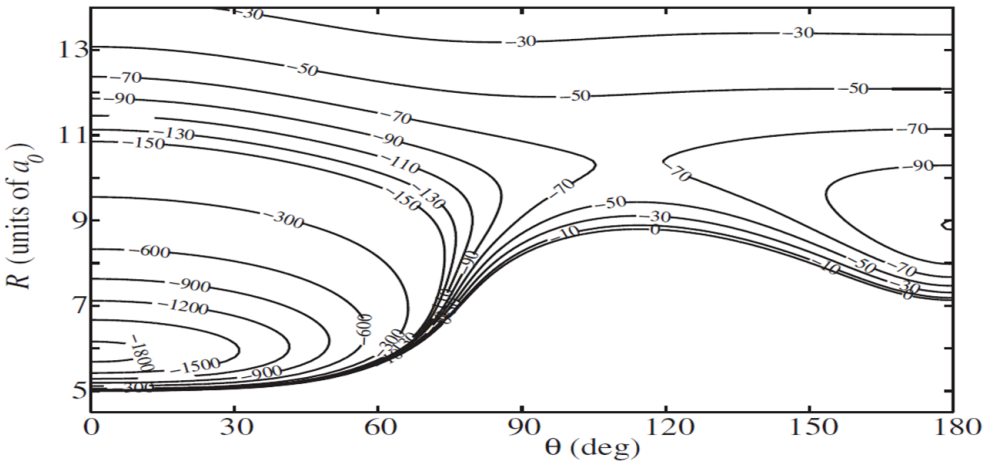

Figure 4.3: Potential energy surface for the Rb-ND_3 interaction from Żuchowski et. al. [24]. The deep well at the interaction angle of 0° is due to the electrostatic interaction of lone-pair site with the Rb.

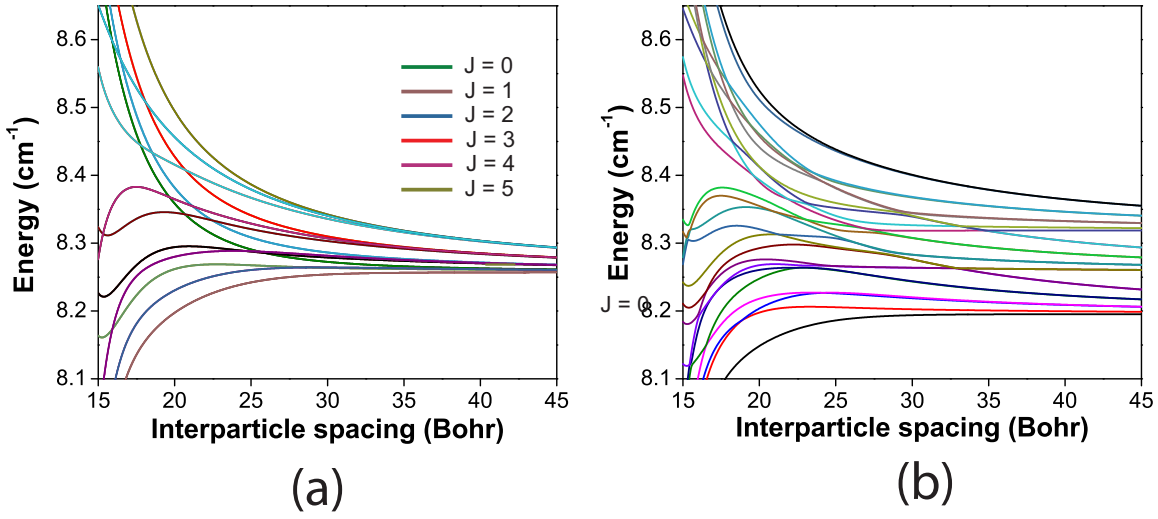

Figure 4.4: The adiabatic curves for the Rb-ND_3 interaction with zero electric field (a) and 5 kV/cm field strength (b). In the absence of electric fields, the adiabats show the curves for different J levels (total angular momentum of the Rb-ND_3 system) cross over each other. Because there are no avoided crossings, the transitions between different J levels are not likely. The presence of an electric field significantly changes the dynamics of the interaction, creating numerous avoided crossings as state with different M become non-degenerate. This results in a greater probability for the ND_3 to change state during the interaction.

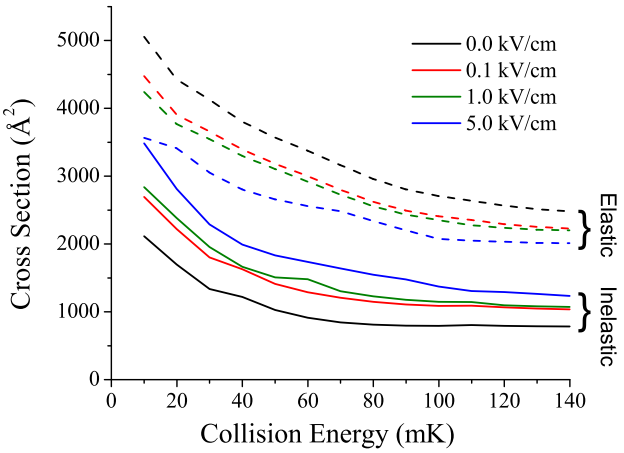

Figure 4.5: Calculated elastic (dashed) and inelastic (solid) cross sections at various electric field strengths.

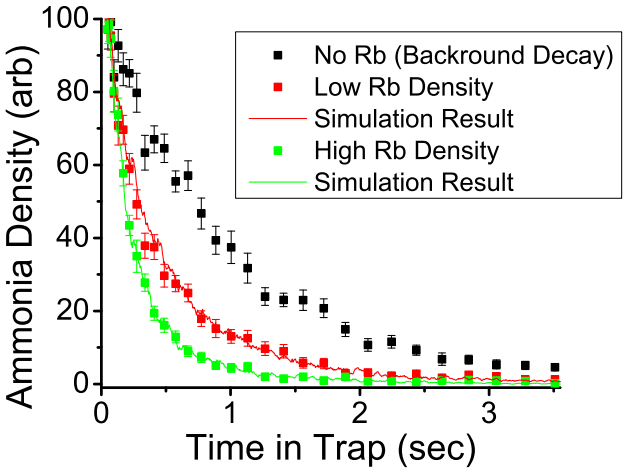

Figure 4.6: ND_3 trap-loss profiles.

axis, determined by the field. At large separations, the electric field is the dominant effect and at short separations, the Rb is the dominant effect. However in the range where the Stark energy and the interaction energy are comparable, around 20 to 30 Bohr, the Rb and ND_3 compete strongly with each other to quantize the ND_3 along different space-fixed axes. This cause the states to mix and creates numerous avoided crossings as is shown in the adiabats in Figure 4.4. Therefore the likelihood of the ND_3 to change state is increased significantly. We therefore expect to see a significant increase in the inelastic cross section with the presence of an electric field

4.2 Measuring Elastic and Inelastic Cross Sections

To extract the elastic and inelastic cross sections, we rely on modeling the collisions of the Rb-ND_3 in the trap using Monte-Carlos simulations. Figure 4.6 shows the ND_3 trap loss profile for two different Rb densities. Also shown are the results from simulation (solid curves) showing good agreement with the data.

There are two reasons for using Monte-Carlos methods to extract the cross sections. First, if the elastic collision rate is large enough, it will have a significant effect on the ND_3 trap decay profile. Because of the significantly colder temperature of the Rb relative to the ND_3, elastic

collisions can result in a significant thermalization of the ND_3 in the trap. This thermalization causes a cooling of the ND_3 and thus an increase in the density of ND_3 at the center of the trap. Measurements of the density of the ND_3 at the center of the trap are used to produce ND_3 decay profiles shown in Figure 4.6. Therefore the actual form that the profiles take on not only depends on the inelastic cross section, but also on the elastic cross section. The elastic and inelastic cross sections can then be extracted by reproducing the measured ND_3 decay profile using models with the elastic and inelastic cross sections as the free varying parameters. Figure 4.7 shows the effect of different elastic cross sections on the trap loss profile, for a given inelastic cross section of $2000\mathring{A}^2$

The second important reason for using Monte-Carlo methods to measure the elastic and inelastic cross sections is specific to this experiment and has to do with the Rb trap itself. In the case where the elastic cross section is small compared the inelastic cross cross section and also having a Rb density that is both uniform in space and constant in time, the inelastic cross section could be analytically determined by fitting the trap-loss profile to a simple exponential. It is, however, not the case the Rb density is uniform and constant. Instead, there are Rb-trap dynamics, which are a result of the electric field [1] , causes the Rb density and size to change while the ND_3 trap lifetime is being measured. Because of these Rb trap dynamics, ND_3 decay is not a simple exponential function and, in fact, is nearly impossible to fit analytically. For this reason, we use Monte-Carlo simulations that include the Rb trap dynamics to reproduce the measured ND_3 trap loss profiles.

4.2.1 Rb Trap Dynamics

Before modeling the ND_3 trap-loss, we must understand what is simultaneously happening to the Rb trap. The Rb trap dynamics are dominated by the dc Stark effect. The Hamiltonian describing this effect is [27]

$$H_s = -\frac{1}{2}\alpha_0 E_z^2 - \frac{1}{2}\alpha_2 E_z^2 \frac{3J_z^2 - J(J+1)}{2(2J-1)} \tag{4.2}$$

[1] The electric field comes from the electrostatic trap

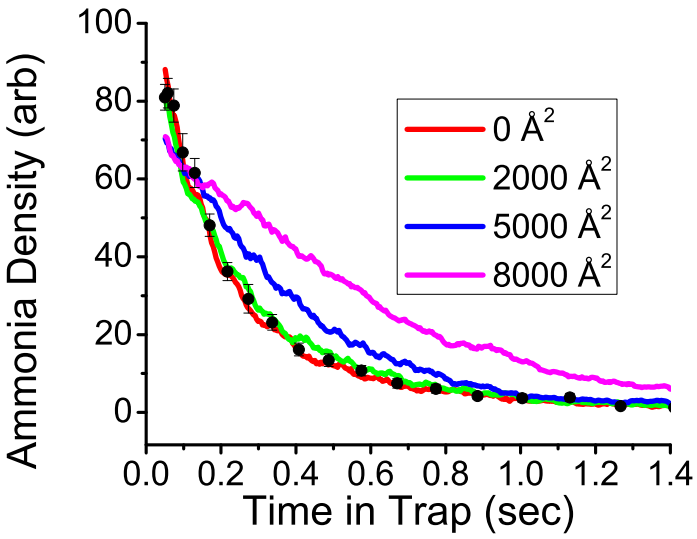

Figure 4.7: Demonstration of the effect of the elastic cross section on the decay profile of the ND_3 trap. These decay profiles (solid lines), which are the results of Monte-Carlos simulations with an inelastic cross section of 2000 Å, show the significant role that the elastic cross section have in the ND_3 trap loss profile. The measured decay profile is also shown (black circles).

where α_0 and α_2 are the scalar and tensor polarizabilities of Rb respectively. The second term vanishes for the case of $J = 1/2$, so the Stark shift is quite simple. The scalar polarizability for the $5S_{1/2}$ state is $\alpha_0 = h \cdot 0.0794$ Hz/(V/cm)^2 [47].

Two-dimensional slices of the trapping Rb trapping potential[2] are shown in Figure 4.8. The slices are in the horizontal plane which is perpendicular to they symmetry axis of the magnetic trap. The two traps are are oriented such that their symmetry axis are perpendicular two each other which also corresponds to the strong axis of the quadrupole electrostatic trap being aligned to the weak axis of the quadrupole magnetic trap. This can be seen in the illustration in Figure 2.13. This particular orientation is unfortunate as it causes the strongest electric field gradients to coincide with the weakest magnetic field gradients, thus significantly lowering the Rb trap walls. It would be better suited if the strong axis of both the magnetic and electrostatic trap could be aligned. Unfortunately due to design constraints, this orientation cannot be achieved. The resultant asymmetry of the net trapping potential is evident in the right hand column of Figure 4.8. The column on the left show the trapping potential at 0, 1, and 2 mm (in the vertical dimension) without the electric field. The right hand column shows the significant amount of distortion cause by the presence of the electric field.

The distortion of the Rb trap due to the electric fields causes the dynamics shown in Figure 4.9. The number of Rb atoms in the trap can be accurately measured using absorption imaging and Figure 4.9(b) shows the observed double-exponential lifetime of the Rb trap with the electric fields present.

Measuring the size of the Rb trap with the electric fields present, however, is not such a trivial task. Typically, the trap size is measured using a ballistic expansion method, where the magnetic fields are abruptly turned off and the Rb cloud is allowed to expand before the image is taken. The initial Rb distribution in the magnetic trap can then be extrapolated by repeating this measurement for a variety of expansion times (typically between 2 and 15 ms). This imaging method however cannot be conducted in the vicinity of the electrostatic trap. The abrupt turning

[2] Potentials modeled in Comsol (www.comsol.com)

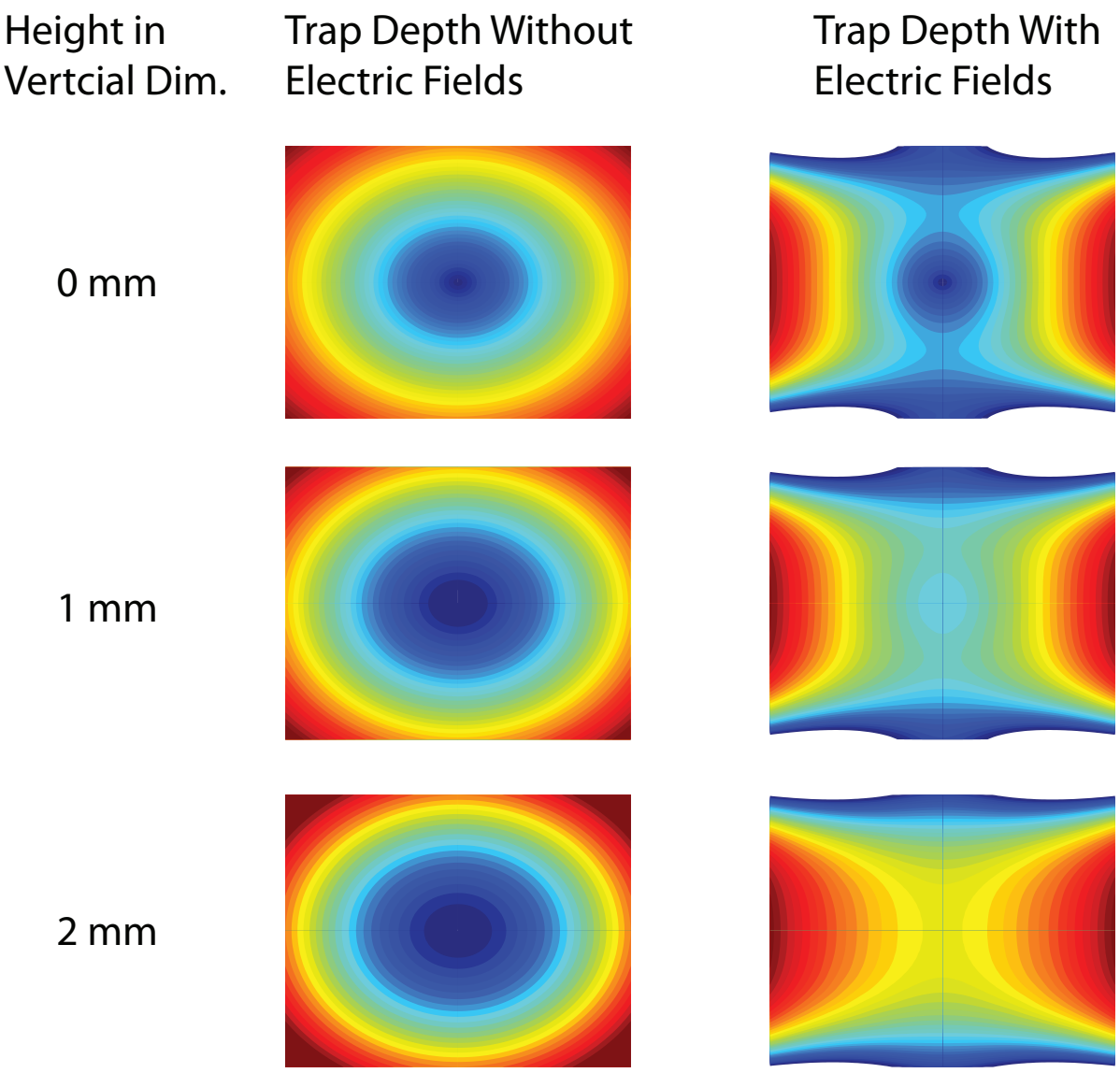

Figure 4.8: Rb trapping potential with and without electric fields.

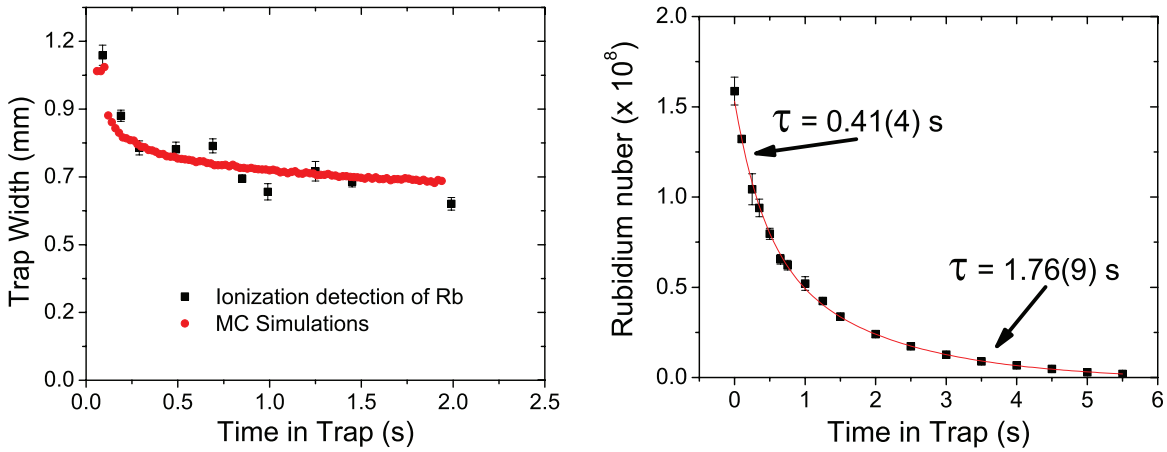

Figure 4.9: Rb trap dynamics. The Rb trap suffers from the electric field generated by the electrostatic trap, causing a double exponential Rb-trap lifetime (right) as well as a time-dependent trap width (left). This trap width is measured in the vertical direction by ionizing the Rb (black squares). Monte-Carlo simulations (red) are run to reproduce this time-dependent width profile and to extrapolate the effect in the other two dimensions.

off of the magnetic fields induces eddy currents in the electrodes of the electrostatic trap that non-uniformly Zeeman shifts the Rb and thus distort the resonant imaging process. Therefore the atoms must be transported away from the electrostatic trap before they can be imaged (this is how the Rb number is measured). Unfortunately, transporting the Rb takes approximately one second during which all information about the Rb distribution in the presence of the electric field is lost.

While we are not able to directly measure the Rb trap distribution in the presence of the electric fields using absorption imaging, we are able to measure the width of the Rb trap in the vertical dimension using a non-resonant detection method. This non-resonant detection method consists of using a focused ultra violet laser to ionize the Rb. The Rb ions are then detected with a micro channel plate detector. The laser is scanned vertically to map out the trap profile as shown in Figure 4.10. Because this method is non-resonant, the inhomogeneous magnetic and electric fields do not affect the detection efficiency. This method however only gives us information about the Rb along a single dimension. In order to have a complete picture of the Rb distribution, we must rely on modeling how the Rb behaves when the electric fields are turned on. Figure 4.9(a) shows the evolution of the vertical width of the Rb trap at the center. The red circles are the result of Monte-Carlo simulations and the black squares are measured widths determined by ionizing the Rb..

The Rb trap dynamics are modeled using a Monte-Carlo method with potentials calculated from a commercially available finite element modeling software package [11]. The Rb-Rb interactions are treated as elastic s-wave scattering events with a scattering length of 95 Bohr and 1900 Bohr for ^{87}Rb and ^{85}Rb respectively [38]. The initial Rb trap distribution is prepared by taking a random sample of velocities and positions (corresponding to kinetic and potential energies respectively) from a Boltzmann's distribution at a temperature of 600 μK. According to the Virial theorem, the mean potential energy in a harmonic potential is equal to the mean kinetic energy.

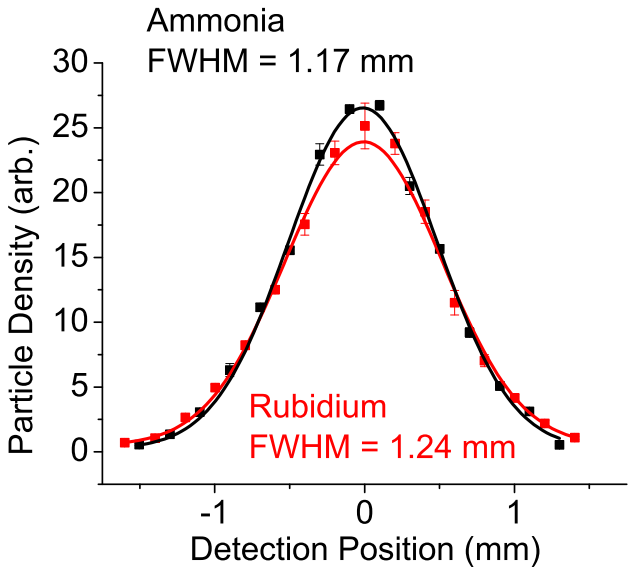

Figure 4.10: Rb (red) and ND_3 (black) trap widths. The trap widths are measured in the vertical dimension by ionizing the Rb or ND_3 .

Table 4.1: Rb trap widths (time dependent)

	Electrostatic Trap Voltage		A_1	τ_1	A_2	τ_2	y_0
^{87}Rb	9 kV	σ_x	8.33e-4	0.066	1.38e-4	0.688	5.04e-4
		σ_y	7.23e-5	0.791	1.88e-4	0.070	3.22e-4
		σ_z	9.24e-5	0.710	5.50e-4	0.050	3.06e-4
	8 kV	σ_x	0.139e-3	1.18	0.742e-3	0.077	0.554e-3
		σ_y	0.084e-3	0.75	0.175e-3	0.071	0.352e-3
		σ_z	0.589e-3	0.05	0.092e-3	1.020	0.344e-3
	7 kV	σ_x	6.57e-4	0.0762	1.64e-4	0.868	6.32e-4
		σ_y	5.02e-4	4.3500	1.23e-4	0.309	3.72e-4
		σ_z	9.90e-5	0.8250	4.97e-4	0.050	3.96e-4
^{85}Rb	8 kV	σ_x	1.76e-4	0.6520	9.27e-4	0.052	6.13e-4
		σ_y	1.70e-4	0.0525	9.85e-5	0.574	4.03e-4
		σ_z	4.21e-4	0.0472	8.84e-5	0.830	3.32e-4

We therefore use the relation in defining the initial distribution,

$$\frac{1}{2}k_{\mathrm{B}}T = \langle E_{\mathrm{kin}}\rangle = \frac{1}{2}m\langle v\rangle^2, \tag{4.3}$$

$$= \langle E_{\mathrm{pot}}\rangle = \frac{2}{5}\mu_0 g\nabla B\langle x\rangle. \tag{4.4}$$

The evolution of the Rb distribution in the trap is represented as a time-dependent three-dimensional gaussian distribution,

$$n(x,y,z,t) = \frac{N_0}{(2\pi)^{3/2}\sigma_x(t)\sigma_y(t)\sigma_z(t)}\exp\left[-\frac{1}{2}\left(\frac{x^2}{\sigma_x(t)^2}+\frac{y^2}{\sigma_y(t)^2}+\frac{z^2}{\sigma_z(t)^2}\right)\right], \tag{4.5}$$

where n is the Rb density, N_0 is the initial Rb number, and $\sigma_x(t)^2$, $\sigma_x(t)^2$, and $\sigma_x(t)^2$ are the time-dependent Gaussian widths in the $x-$, $y-$ and $z-$dimensions respectively. The time dependence of the widths has a double exponential behavior given by,

$$\sigma(t) = A_1 \mathrm{e}^{t/\tau_1} + A_2 \mathrm{e}^{t/\tau_2} + y_0, \tag{4.6}$$

where the constants, A_1, τ_1, A_2, $\tau 2$, and Y_0, determined from Monte-Carlo simulations,

Table 4.2: Rb lifetimes

	Electrostatic Trap Voltage	A_1	τ_1	A_2	τ_2	y_0
^{87}Rb	9 kV	2.01e8	.79	2.59e8	.05	2.8e6
	8 kV	3.35e8	.84	1.24e8	.04	5e6
	7 kV	4.6e8	.91	0	0	9.57e6
^{85}Rb	8 kV	6.64e7	.85	1.66e7	.03	5e6

are listed in Table 4.1. In addition to the widths, the Rb lifetime is also fit to the same double exponential formula in Equation 4.6 with the constants listed in Table 4.2

4.3 Modeling the Rb-ND_3 Co-Trap

In modeling the ND_3 -Rb trap, the initial ND_3 distribution is derived from Monte-Carlo simulations of the trap loading. This is important because the the actual ND_3 distribution is far from thermal and cannot be simply approximated by a Boltzmann distribution for a given temperature. Instead the distribution is set by the coupling between the phase-space acceptance of the electrostatic trap-loading process and the phase-space distribution of the ND_3 as it exits the decelerator. Because the ND_3 density is very low, the ND_3 -ND_3 collision rate is also very low and thus the trap does not obtain thermal equilibrium during the time scale of the Rb-ND_3 interaction. Figures 4.12 through 4.13 show the position and velocity distributions in the the electrostatic trap after the loading sequence described in § 2.2.1. Although the trap is cylindrically symmetric, the x- and y-distributions (for both position and velocity) do not exhibit this symmetry. This is because Stark decelerator does not share this cylindrical symmetry and the x-v_x and y-v_y phase space is set by the orientation of the final electrodes in the decelerator. Figure 4.13 shows the "holes" in the z-v_z phase space distribution of the trap. These holes are a result of the particularly poor phase-space matching between the Stark decelerator and the trap. Techniques have been demonstrated, using a *buncher* [51], to rotate the phase space of the molecules after they exit the decelerator in order that it better matches the phase space acceptance of the trap. However, because the physical geometries of the decelerator and the trap are significantly different, getting perfect phase-space

matching is nearly impossible.

The ND_3 distributions extracted from the trap loading simulations and the Rb distributions, parameterized in Table 4.1 and 4.2, are combined to model the ND_3 trap loss profile to determine the Rb-ND_3 cross sections. The trap loading simulations are part of a separate Monte-Carlo that simulates the deceleration of a packet of molecules in the Stark decelerator. The fields in the Stark decelerator are modeled using the commercial finite-element modeling software, Comsol. The timing of the simulated decelerator is set to match the timing of the experiment. The initial distribution of the molecules as they enter the decelerator is empirically determined. The parameter space for the initial molecule distribution includes longitudinal velocity (v_z), longitudinal velocity spread (δv_z), radial velocity spread (δv_r), longitudinal position spread (δz), radial position spread (δr), and the distance from the valve to the entrance of the decelerator (d). The values of these parameters are set by the supersonic expansion and are determined by experimentally decelerating the molecules to different final speeds and matching the resulting time-of-flight traces with simulated time-of-flight traces. The best values for the above parameters are

$$\begin{aligned} v_z &= 415 \text{ m/s} \\ \delta v_z &= 60 \text{ m/s} \\ \delta v_r &= 5 \text{ m/s} \\ \delta z &= 0.03 \text{ m} \\ \delta r &= 0.3 \text{ m} \\ d &= 0.4 \text{ m}. \end{aligned}$$

The radial position spread is chosen to be quite large because the radial distribution of the molecules entering the decelerator is basically uniform. Using the above parameters, the molecular distribution is modeled throughout the decelerator and trap loading sequence. The resulting trap distribution is then used as inputs into the Rb-ND_3 trap to model the ND_3 trap loss profile.

To model the ND_3 trap loss profile, close to 1000 simulations are run with varying elastic and inelastic cross sections. Integrating the equations of motion for the ND_3 trajectories is done using

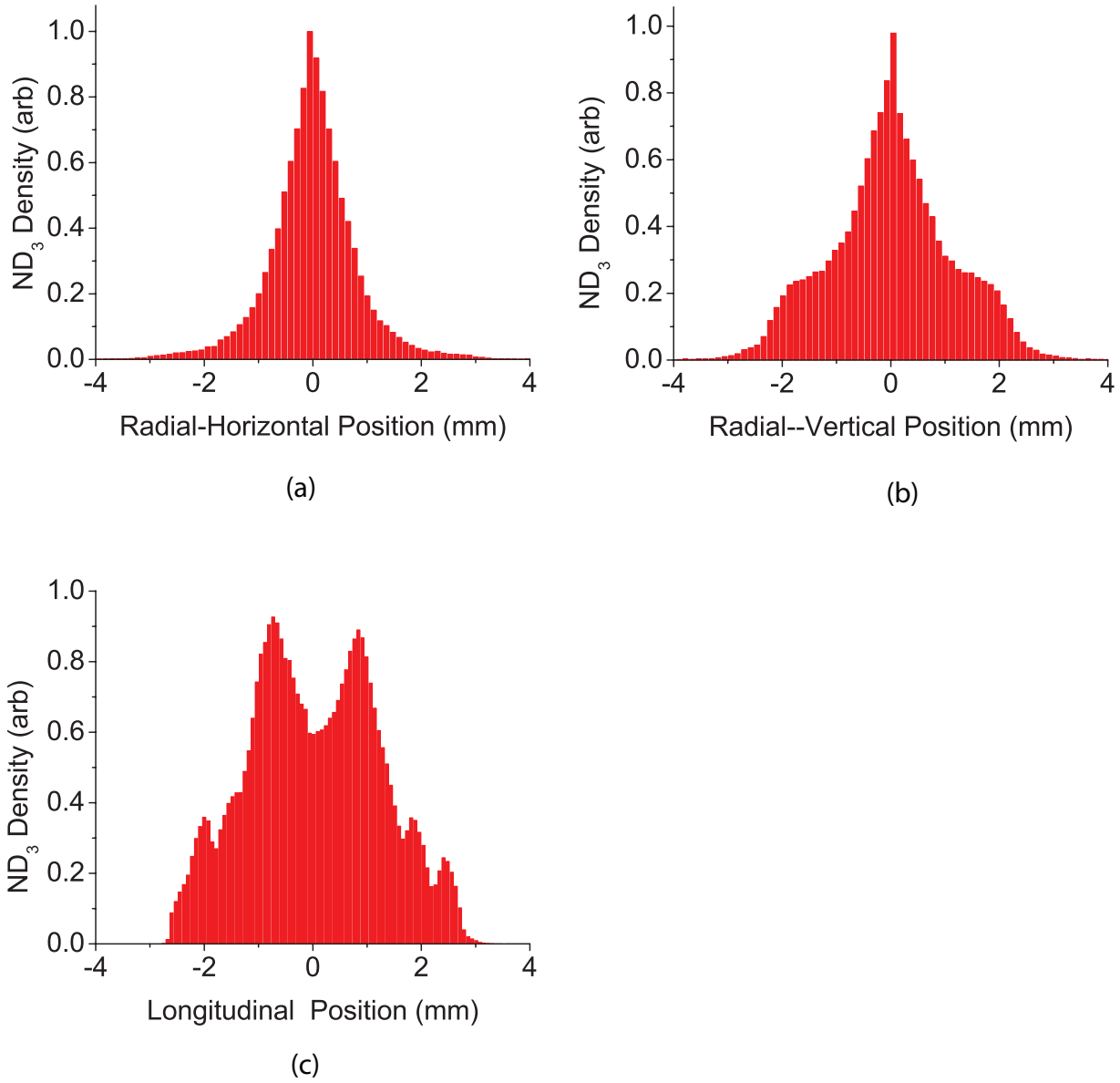

Figure 4.11: ND_3 distributions in the electrostatic trap.

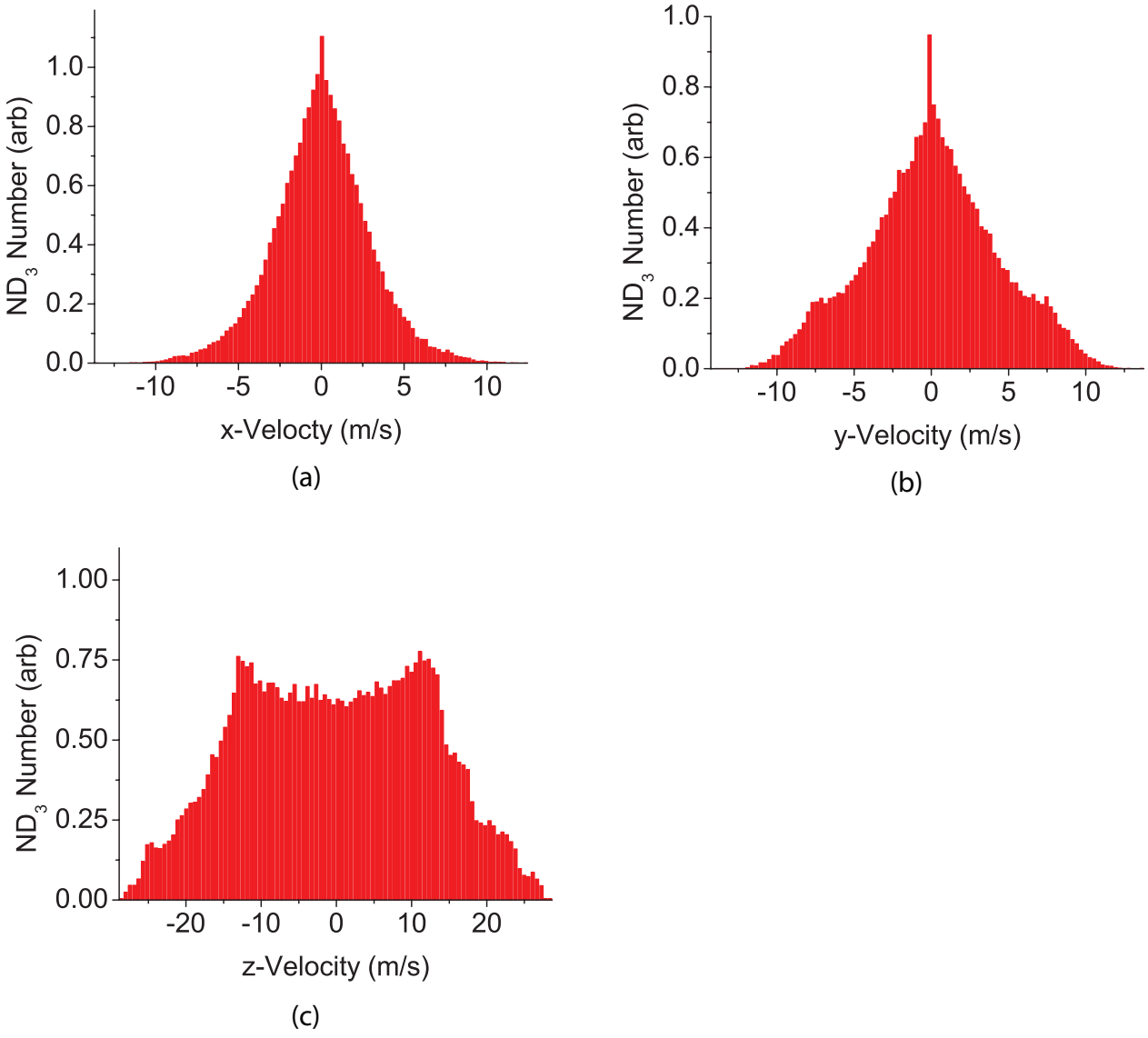

Figure 4.12: ND_3 velocity distribution vs position in the electrostatic trap.

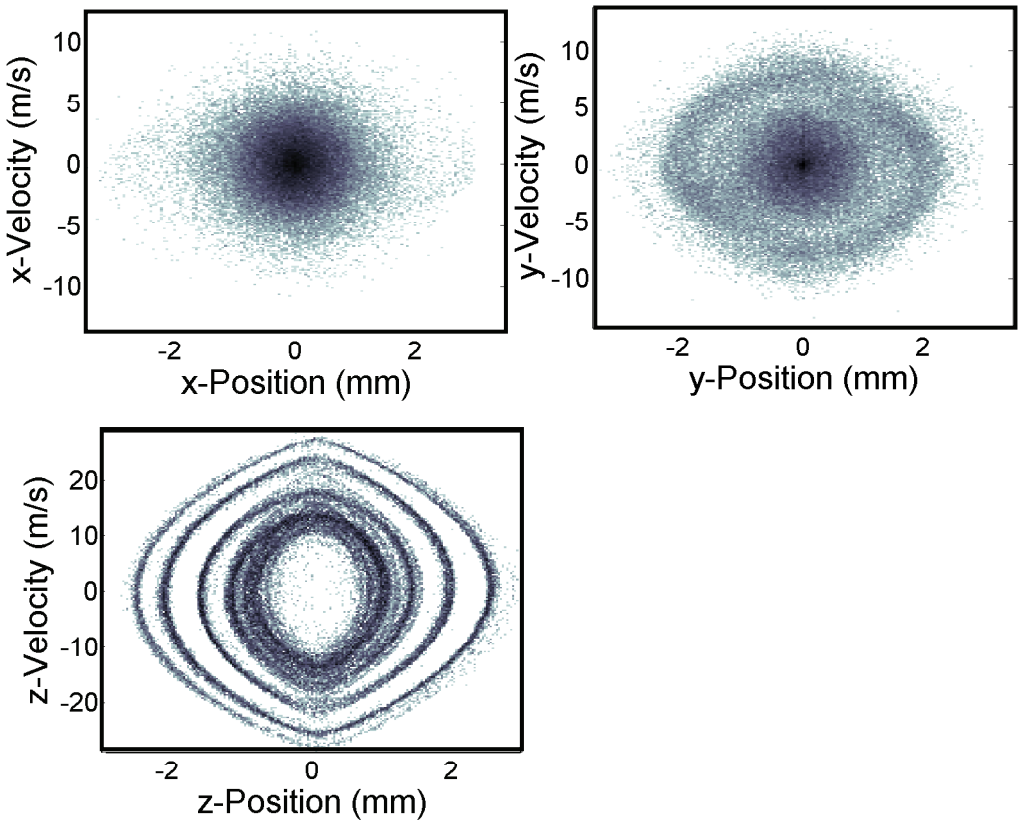

Figure 4.13: ND_3 phase space distributions in the electrostatic trap.

a *position extended Forest-Ruth like* (PEFRL) algorithm [35]. The PEFRL algorithm is a fourth order verlet integration method that offers greater stability than the simpler Euler or Runge-Kutta integration methods.

$$\begin{aligned}
\mathbf{r}_1 &= \mathbf{r}(t) + \xi h \mathbf{v}(t) \\
\mathbf{v}_1 &= \mathbf{v}(t) + (1-2\lambda) h \mathbf{F}(\mathbf{r}_1)/2m \\
\mathbf{r}_2 &= \mathbf{r}_1 + \chi h \mathbf{v}_1 \\
\mathbf{v}_2 &= \mathbf{v}_1 + \lambda h \mathbf{F}(\mathbf{r}_2)/m \\
\mathbf{r}_3 &= \mathbf{r}_2 + (1 - 2(\chi + \xi))\, h \mathbf{v}_2 \\
\mathbf{v}_3 &= \mathbf{v}_2 + \lambda h \mathbf{F}(\mathbf{r}_3)/m \\
\mathbf{r}_4 &= \mathbf{r}_3 + \chi h \mathbf{v}_3 \\
\mathbf{v}(t+h) &= \mathbf{v}_3 + (1-2\lambda) h \mathbf{F}(\mathbf{r}_4)/2m \\
\mathbf{r}(t+h) &= \mathbf{r}_4 + \xi h \mathbf{v}(t+h),
\end{aligned} \tag{4.7}$$

where h is the time step, $\mathbf{F}(\mathbf{r})$ is the force on the molecule at position $\mathbf{r}$, and the constants ξ, λ, and ξ are,

$$\xi = 0.1786178958448091$$

$$\lambda = -.2123418310626054$$

$$\chi = -0.06626458266981849.$$

The greater stability of the PEFRL method is important to maintain the phase space distribution over the long trap time. Also its increased efficiency allows for much greater step size making the task of running all the sims necessary to determine the Rb-ND_3 cross sections for each isotopic combination and at three different field strengths much more feasible. Fifty thousand ND_3 molecules are simulated with step size of 10 μs for four seconds. Each simulation takes between five and twenty minutes to complete, depending on the size of the cross sections, using eight 2.8 GHz Intel Xeon processors.

The ND_3 trap-loss profile from each simulation is compared against the trap loss profile from the experiment and a *fitness level* is computed which states how well the result of each simulation matches the experimental result. This fitness level is simply the reduced χ-square,

$$\chi^2_{\text{reduced}} = \frac{1}{\nu} \sum_i \frac{[h_s(i) - h_e(i)/\delta h_e(i)]^2}{\delta h_e(i)^2}, \tag{4.8}$$

where ν is the number of degrees of freedom given by $N - n - 1$, where N is the number of points measured (i.e. number of observations) and n is the number of fitted parameters (two in this case for elastic and inelastic cross sections), $h_e(i)$ is the experimentally determined ND_3 density at time $t = t_i$, $\delta h_e(i)$ is the corresponding error of the measurement, and $h_s(i)$ is the simulated ND_3 density at $t = t_i$. As a general rule a value of $\chi^2_{\text{reduced}} = 1$ is an ideal result [12]. If $\chi^2_{\text{reduced}} \gg 1$ means a poor fit and indicates that the model does not properly reproduce the system. On the other hand, if $\chi^2_{\text{reduced}} \ll 1$, then the fit is "too good" and either the model is incorrect or the errorbars have been overestimated.

To compare the simulated and measured trap-loss profiles, a scaling factor must first be introduced. This scaling factor then relates the ND_3 density measured in the simulation to that measured in the experiment. Unfortunately our REMPI detection method does not tell us the number of molecules in the trap[3] . Thus the scaling factor is not a number which can be directly measured. Instead a scaling factor is introduced for each individual simulation in such a way that it minimizes the reduced chi-square for that simulation using a nonlinear least-squares minimization function.

4.4 Results

The measured elastic and inelastic cross sections are presented as contour plots in Figures 4.15 and 4.17. Figure 4.15 show three contour lines that show the confidence bounds at the 1σ (68%), 2σ (95%), and 3σ (99.7%) levels. These contour levels represent lines of constant *reduced*–χ^2, where the

[3] The cross section of the REMPI transition is not known. Also the gain of the MCP detector is not known to better than an order of magnitude (and decreases with the age of the detector). Therefore we are really only measuring *relative* densities.

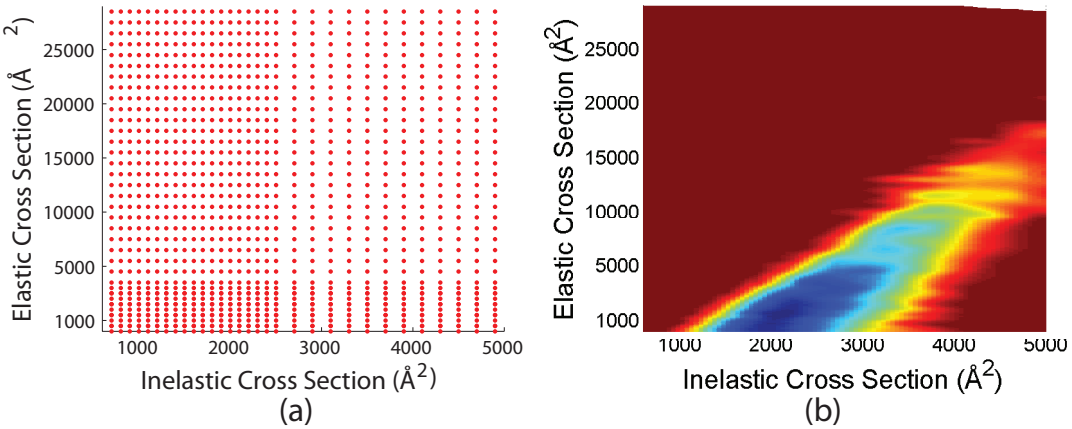

Figure 4.14: Grid points of simulations run (a) and false-color image of the resulting χ^2_{reduced} (b). Each grid point represents an elastic/inelastic cross section combination for which a simulation was run. Each simulation generates a ND_3 trap loss profile, such as the ones shown in Figure 4.19 and the combination of all simulations generate the contours shown in Figures 4.15 and 4.17.

reduced–χ^2 represent how well the the simulation matches the data. The value of the 1σ, 2σ, and 3σ contour levels are $2.3\chi^2_{\text{min}}$, $5.99\chi^2_{\text{min}}$, and $11.6\chi^2_{\text{min}}$ respectively, where χ^2_{min} is the the minimum *reduced*–χ^2 for the entire system (i.e. the *reduced*–χ^2 for the best matched simulation), which for this case is 1.2. The green dot in Figure 4.15 indicates the theoretically predicted value of the elastic and inelastic cross sections in zero electric field ($\sigma_{\text{elastic}} \approx 2700\mathring{A}^2$ and $\sigma_{\text{inelastic}} \approx 790\mathring{A}^2$), which corresponds to a statistical p-value of $< 10^-5$.

The precision with which the inelastic cross section is measured is quite good with a 1σ width of roughly 900 Å^2. The elastic cross section however, is predicted with less precision. As discussed earlier, the precision with which the elastic cross section can be measured depends on the ratio of the elastic to inelastic cross sections. At best an upper limit can be placed on the elastic cross section of approximately a factor of 2.5 greater than the inelastic cross section, determined by the slope of the contours in Figures 4.15 and 4.17.

We also measure the cross sections at different average electric field strengths by changing the trapping voltage applied to the electrostatic trap. Figure 4.5 shows the effect on the cross section as with different electric field strengths. The elastic cross section is shown to decrease as the electric field is increased, while the inelastic cross section increases with electric field strength. It is not shown in this plot, however the the electric field dependence on the cross section plateaus above 5 kV/cm. In other words, above 5 kV/cm, the the elastic and inelastic cross sections do not change. Unfortunately, we do not have very much flexibility to adjust the electric field strength as it is coupled to our trapping potential. If we reduce the field strength too far, we cannot trap the molecules and if we go too high in the field, we develop high-voltage breakdown issues across the electrodes. Over the range which we are able to adjust the electric field strengths, we see no significant difference as shown in Figure 4.7. Figure 4.18 shows the density of ND_3 that samples various electric field strengths with a green line indicated the saturation threshold. From this figure, it is evident that we cannot significantly effect the distribution of ND_3 below the 5 kV/cm threshold and therefore should not expect to see a variation in the cross section at this level.

The confidence bounds shown by the contour intervals in these figures are solely statistical

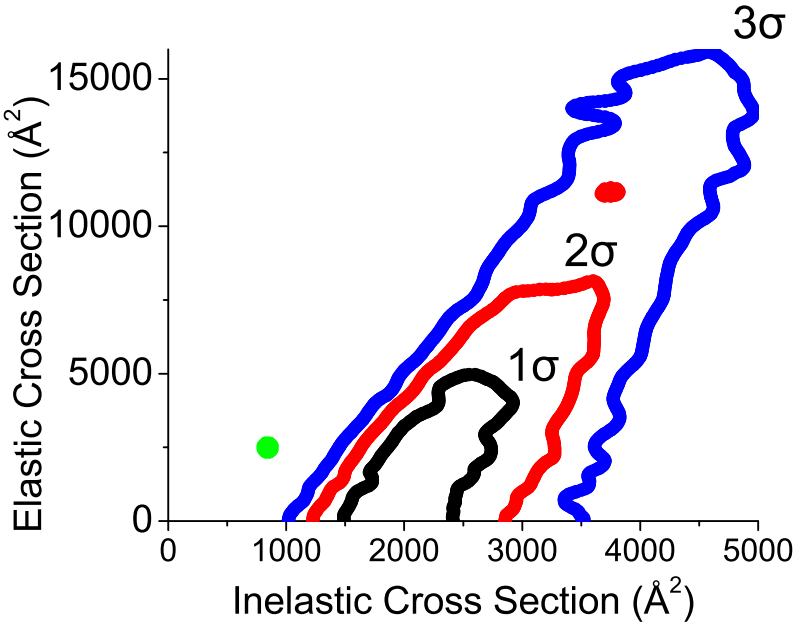

Figure 4.15: Elastic and inelastic cross section for the ^{87}Rb-^{14}ND$_3$ system. The contours indicate the 1σ (68%), 2σ (95%), and 3σ (99.7%) levels. The green dot indicates the theoretical prediction for the elastic and inelastic cross section in zero electric field.

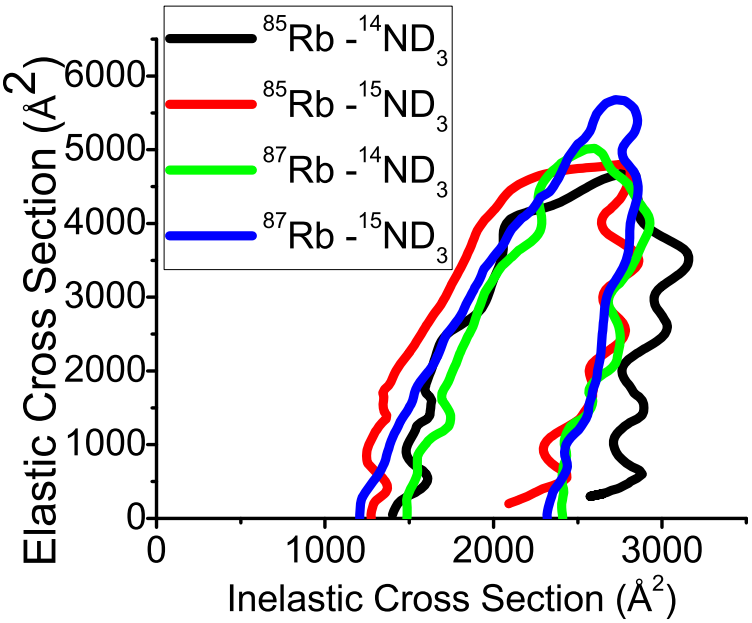

Figure 4.16: 1σ confidence bounds for the elastic and inelastic cross sections with different isotopic combinations of the Rb-ND$_3$ system.

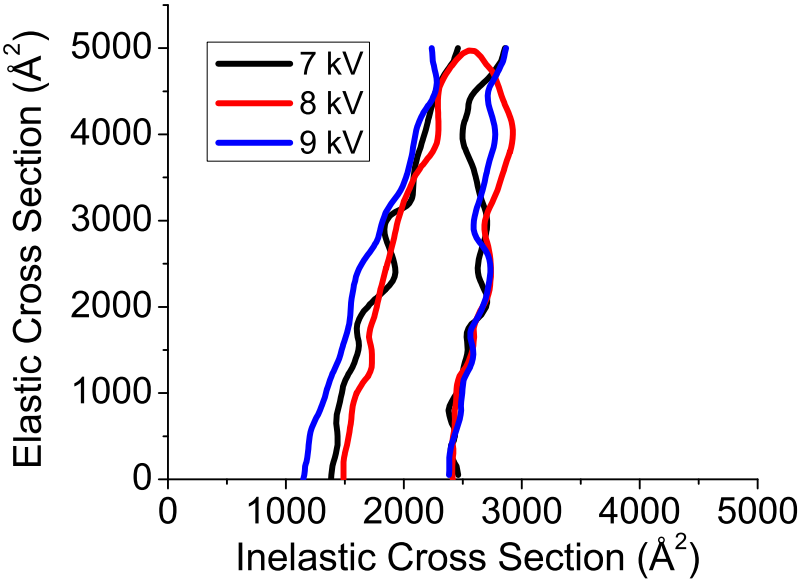

Figure 4.17: 1σ confidence bounds for the elastic and inelastic cross sections with different electric field strengths applied to the trap electrodes. Varying the electric field over this range does not significantly affect the number of molecules below the electric field saturation limit of the inelastic cross section. Therefore we do not expect to be able to see an effect on the inelastic cross section

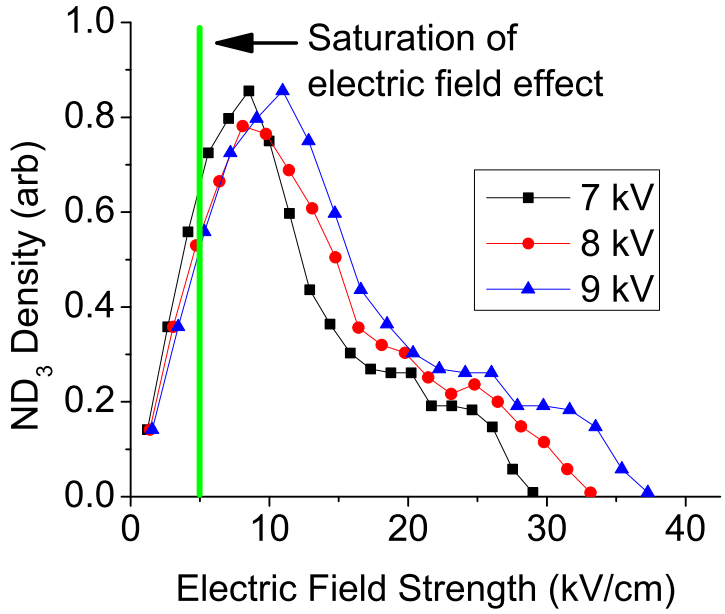

Figure 4.18: Plot of the the field strength sampled by the ND_3 for three different electrostatic trap voltages. The green line indicates where the electric field effect on the Rb-ND_3 3 interaction reaches a saturation level. Above 5 kV/cm, increasing the electric field no longer changes the inelastic cross section.

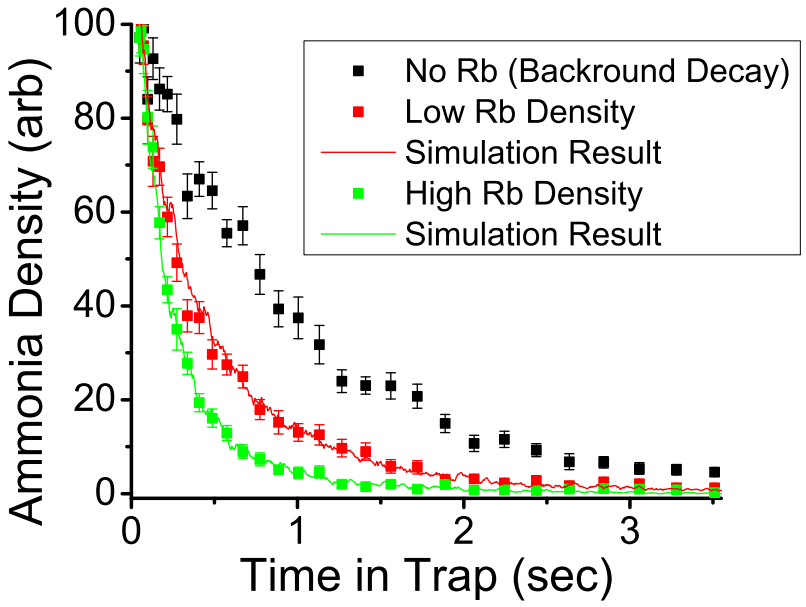

Figure 4.19: ND_3 trap loss profiles. The measured ND_3 trap loss profiles are shown along with the best matched results from Monte-Carlo simulations. The simulation results match the measured data with a $\chi^2_{reduced} \approx 1.2$, indicating strong agreement between the model and the data.

and do not include the uncertainties in various parameters including the rubidium lifetime, width, or density. To understand the significance of these uncertainties, the same Monte-Carlo simulations used to determine the cross-sections are rerun with different values input for the various parameters. The parameter values are varied by $\pm 10\%$ which, for all parameters, corresponds to approximately a 1σ deviation from the expected value. Figure 4.20 show the effect on the confidence bounds as a result of changing these parameters in the simulations. One interesting note on the results of these simulations is that the contour lines indicate a greater level of uncertainty when value of the input parameters are chosen to be $\pm 1\sigma$ from the expected value. This is because when the parameters such as the Rb width or lifetime are incorrect, the model no longer accurately represents the experiment and the value of χ^2_{min} increases. And a greater value of χ^2_{min} results in a greater level of uncertainty in the measurement.

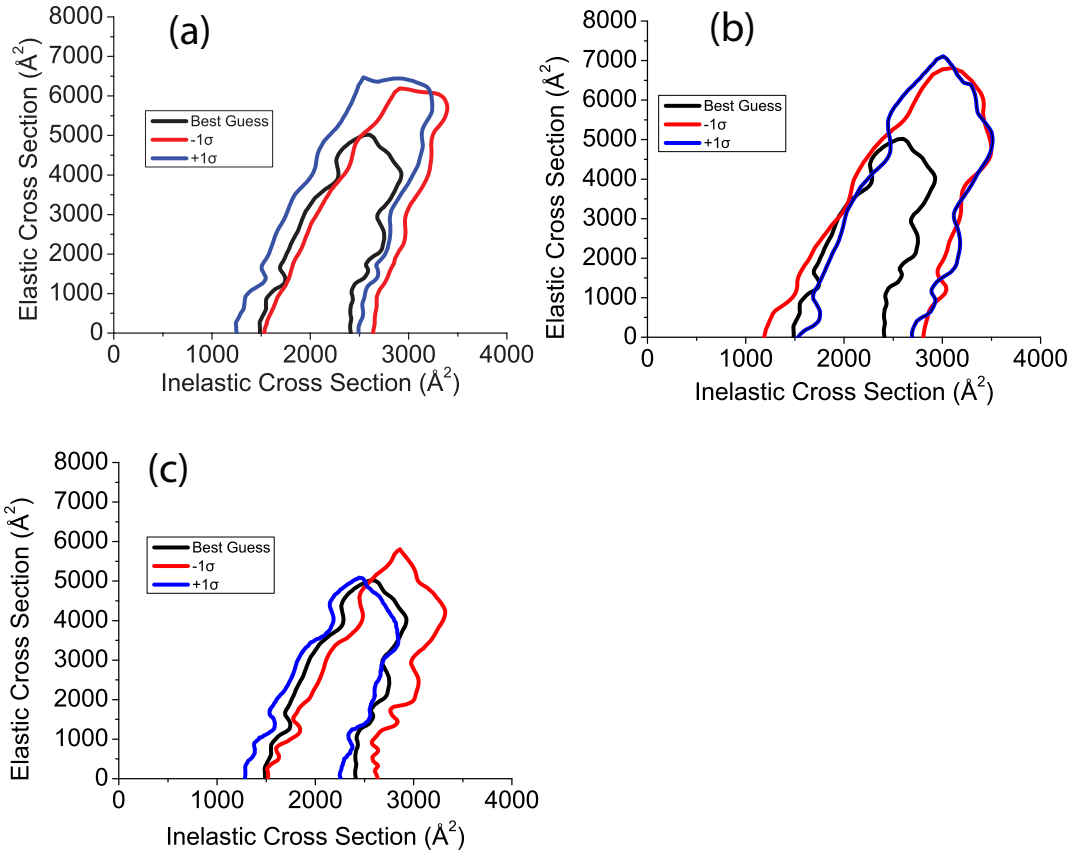

Figure 4.20: Effects of varying different parameters in the Rb-ND_3 simulations. The Rb density (a), Rb lifetime (b), and Rb width (c) are varied by $\pm 1\sigma$ to determine their effect on the measured cross section.

Chapter 5

Using Stark Decelerator for High-Resolution Molecular Beam Studies

The following text is from an article we published in New Journal of Physics in May 2009. In this article we describe an alternate method of operating a Stark decelerator that further reduces the energy spread over the standard method of operation. In this alternate mode of operation, we aggressively decelerate the molecular packet using a high phase angle. This technique brings the molecular packet to the desired velocity before it reaches the end of the decelerator; the remaining stages are then used to longitudinally and transversely guide the packet to the detection/interaction region. The result of the initial aggressive slowing is a reduction in the phase-space acceptance of the decelerator and thus a narrowing of the velocity spread of the molecular packet. In addition to the narrower energy spread, this method also results in a velocity spread that is nearly independent of the final velocity. Using the alternate deceleration technique, the energy resolution of molecular collision measurements can be improved considerably.

5.1 Introduction

Cold molecular beams created from supersonic jets have been used extensively to study gas-phase reaction dynamics and molecular interactions [44, 31, 45]. Crossed molecular beams are responsible for a large part of our understanding of bimolecular gas-phase reactions. In these systems, molecular beams are created with temperatures as low as 1K with only a few quantum states occupied. This control over internal and external degrees of freedom is necessary to explore the detailed nature of molecular collisions. One parameter that has not been under precise control

until recently is the mean velocity of the beam and thus the collision energy. Typical molecular beams can be produced with mean speeds ranging from 300–2000 m/s in large incremental steps depending on the carrier gas used in the expansion. This coarse speed control does not allow experimental studies of narrow collision resonances and thresholds [22, 28]. More recently, crossed-molecular-beam experiments were built in which the relative angle between the beams could be adjusted to allow the collision energy to be changed [19, 46]. These experiments, however, have an energy resolution that is limited by the velocity spread in the initial beam, which is particularly poor at small collision energies.

With the advent of the Stark decelerator, we can now continuously tune the speed of a pulsed molecular beam using time-varying inhomogeneous electric fields [6]. In addition, the nature of the Stark decelerator allows the energy resolution of the beam to be increased greatly. This control enables a new range of molecular collision experiments [17, 42]. Many groups around the world have built experiments based around a Stark decelerator, all of which have the same basic configuration [6, 9, 10]. In addition to the standard configuration, which we use for this paper, there are also optical and magnetic analogs [3, 34] as well as alternating gradient decelerators for decelerating high-field-seeking states [4, 48] as well as low-field seeking states [57]. We describe an alternate mode of operation of a typical decelerator that optimizes the energy resolution for molecular collision experiments.

5.2 Standard Stark deceleration

The Stark deceleration process uses the interaction of an electric field with a molecule's dipole moment to decelerate a portion of a molecular beam. The pulsed beam of molecules is prepared via supersonic expansion in the ground ro-vibrational state in either a ground or metastable electronic state. After the beam is expanded fully, the molecules propagate into a region of the vacuum system containing a series of high-voltage electrode pairs. The geometry of the electrodes creates a maximum of the electric field in the longitudinal direction directly between an electrode pair. The molecules slated for deceleration are in a quantum state that increases in energy with increasing

electric field. As these molecules propagate into the increasing electric field, longitudinal kinetic energy is converted to potential energy. If the molecules were allowed to continue down the potential hill, they would regain the lost kinetic energy as they exited the high electric field; however, before they begin to accelerate, the electric field is turned off nearly instantaneously (< 100 ns), thus removing energy from the molecules. We repeat this process with successive stages of electrodes until the molecules have been slowed to the desired speed. Transverse guidance of the molecules is achieved because the molecules are attracted to the minimum of the electric field along the center of the decelerator. Successive electrode pairs are orientated orthogonally to one another to guide the molecules equally in both transverse dimensions.

The final velocity of the molecular packet is determined by the amount of energy removed per slowing stage and the number of stages. The farther up the potential hill the molecules travel before the field is switched, the more energy is removed from the packet. It is typical to parameterize the position of the synchronous molecule when the field is switched in terms of a phase angle, ϕ_0 [7]. A phase angle of $\phi_0 = 0^\circ$ corresponds to no energy being removed from the packet, whereas a phase angle of $\phi_0 = 90^\circ$ corresponds to the maximum possible energy being removed. For a particular phase angle, there exists a phase-space acceptance of the decelerator in both position and velocity. The acceptance of the decelerator is the phase-space volume that will be stably slowed and transported to the end of the decelerator. This phase-stable volume can be illustrated through the use of a separatrix (figure 5.1). Figure 5.1 shows the phase-stable portion of the molecular beam decreases rapidly with increasing phase angle. Although large phase-angle slowing reduces the total number of molecules in the packet, it also reduces the velocity spread. We take advantage of this reduced velocity spread in our alternate slowing protocol to produce tunable molecular beams with narrow energy spreads for collision studies.

We demonstrate the new slowing method with our experimental apparatus shown in figure 5.2. It includes a pulsed valve that produces a beam of ND_3 molecules seeded in krypton. The mean speed of the beam is 415 m/s with a longitudinal velocity width of 28%. After the expansion, the beam enters a differentially pumped chamber containing a 149-stage Stark decelerator operated at

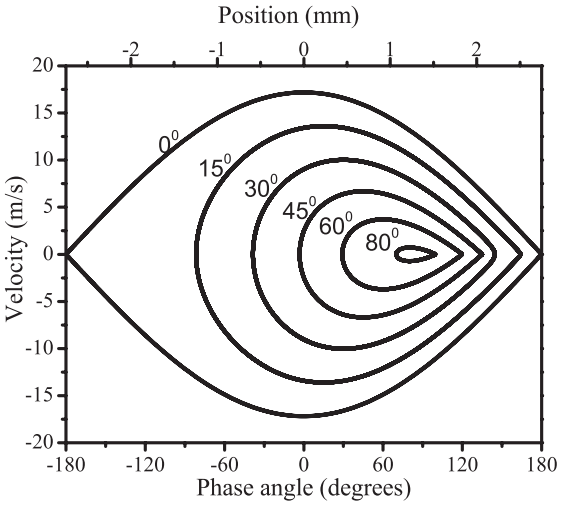

Figure 5.1: Separatrix for the ND_3 molecule in our Stark decelerator. The separatrix curve shows the boundary between the stable and the unstable phase space for a variety of different slowing angles. Molecules within the separatrix curve will be slowed and transported to the end of the decelerator. The separatrix only takes into account the longitudinal dimension of the phase space.

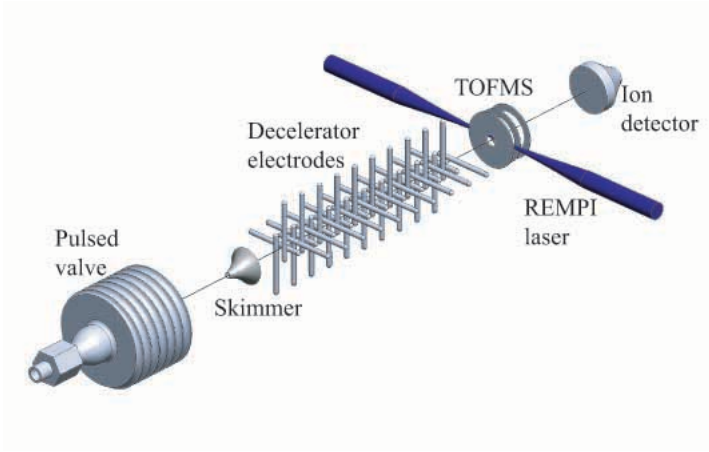

Figure 5.2: Experimental set-up. It consists of a PZT-driven pulsed valve, molecular beam skimmer, decelerator stages, linear time-of-flight mass spectrometer (TOFMS), and a microchannel-plate ion detector. The decelerator consists of 150 electrode pairs (not all are shown).

$\pm$ 12 kV. At the exit of the decelerator, the molecules are ionized using a focused beam from a pulsed dye laser operating around 317 nm via a 2+1 resonance enhanced multi-photon ionization (REMPI) process. The ions are then accelerated towards a microchannel plate detector by a Wiley-McLaren style time-of-flight mass spectrometer [56].

5.3 Alternate deceleration method

To develop efficient slowing protocols, we begin with three-dimensional (3D) Monte-Carlo simulations to understand fully the phase-space dynamics of the deceleration process. Full 3D simulations are required as the separatrix is only a one dimensional representation of the stable phase-space. As pointed out in Refs. [43, 40], the transverse velocity and position dimensions modify the phase-space acceptance of the decelerator.

This effect can be seen very clearly in our experiment for the case of bunching ($\phi_0 = 0°$). Figure 5.3 shows a time-of-flight profile of the bunched molecular beam including the corresponding simulations. From the plot of the occupied phase space, shown in figure 5.3(a), one can see the separatrix is not filled uniformly. There are features in the distribution that are considerably more narrow than the characteristic length scale of the decelerator. Although our ionization-detection scheme essentially integrates this distribution through the velocity dimension, we can still probe this detailed structure experimentally in the position dimension. The structure within experimental signal is elucidated by the simulated phase-space distribution and shows excellent agreement with the 3D simulations. With this agreement, we are confident that our simulations accurately predict the phase-space distribution and thus the energy spread within our slowed molecular packet. This understanding is critical because we can not measure directly the velocity distribution of our molecular beam.

The standard method to run a Stark decelerator is to choose a phase angle such that the molecular packet is at the desired velocity when it exits the last stage of the decelerator. With this method, the energy width of the slowed packet can be relatively large for high mean velocities as it is determined by the phase angle and thus depends on the final velocity. For the method we

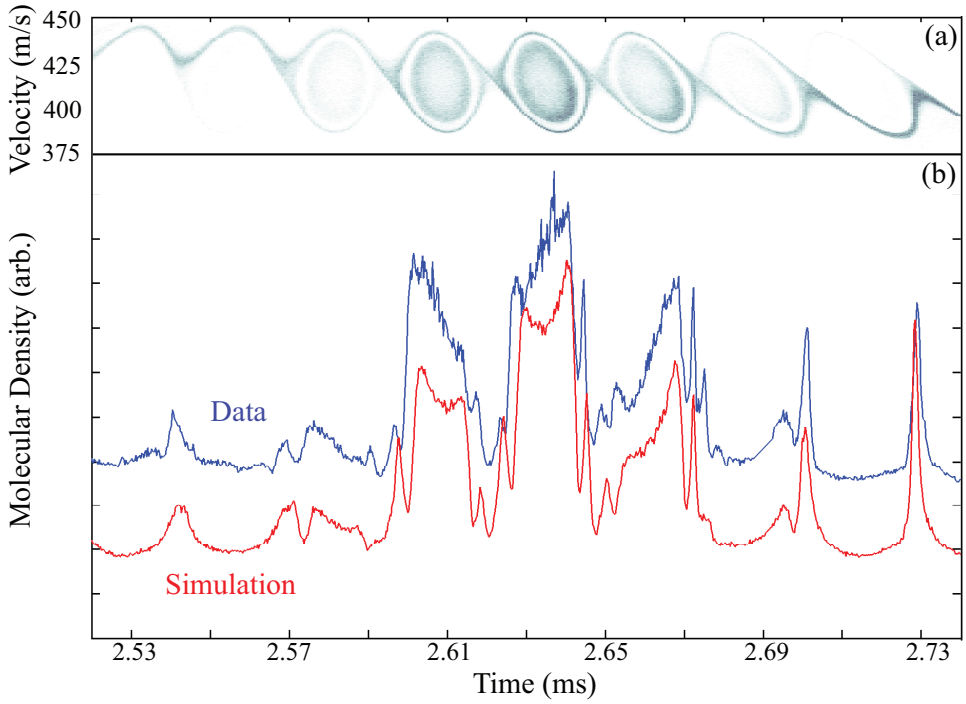

Figure 5.3: Bunching data.(a) Phase-space distribution for bunching ($\phi_0 = 0°$). (b) A time-of-flight (ToF) trace (blue) is shown with the results of a 3D Monte-Carlo simulation (red). The horizontal axis for both (a) and (b) is the ToF to the detection laser, which is 1.8 cm past the end of the decelerator.

propose, a large phase angle is chosen ($\phi_0 = 80^\circ$ in our case), and the number of slowing stages is chosen to decelerate to the final velocity. Once the molecular packet has reached desired velocity, the decelerator is operated in bunching ($\phi_0 = 0^\circ$) mode to guide the packet to the end of the decelerator while maintaining the desired velocity. Figure 5.4 illustrates the difference between the standard and alternate methods. In figure 5.4(a), the time the molecules spend in a stage of the decelerator as they propagate is plotted for several different final velocities. In the standard method, the molecules are slowed progressively for the entire 149 stages at a different phase angle depending on the desired final velocity. The time spent in a stage increases as the molecules are decelerated. With the alternate slowing technique, the molecules always follow the same trajectory until they reach the desired velocity at which point the switching time of the decelerator remains constant indicating a constant velocity.

One advantage of the alternate slowing protocol is the increased time between the arrival of the slowed packet and the unslowed beam. This is important for two reasons. First, for relatively large velocities, the slowed packet will ride on a background of the unslowed molecules, thus increasing the energy spread. This effect can be seen in figure 5.5(b) where a packet slowed to 200 m/s with the standard protocol has not separated completely from the unslowed beam. For this case, the unslowed molecules can not be distinguished from the slowed packet. This overlap is undesirable for collision experiments in which collision energy plays a role. Second, it is advantageous to have sufficient time between the unslowed beam and the decelerated molecules to insert another collision reactant into the path. In the case of collisions between trapped atoms or molecules and a slowed beam of molecules, the trapped reactant can be moved into position after the unslowed beam has gone by, thus reducing unwanted collisions with the unslowed beam. An example of this increased separation is shown in figure 5.5, where we slow a portion of the molecular beam to 200 m/s using both the standard slowing technique and the alternate method. Here we see the arrival time between the unslowed beam and the slowed packet has increased by 0.5 ms. This increase in

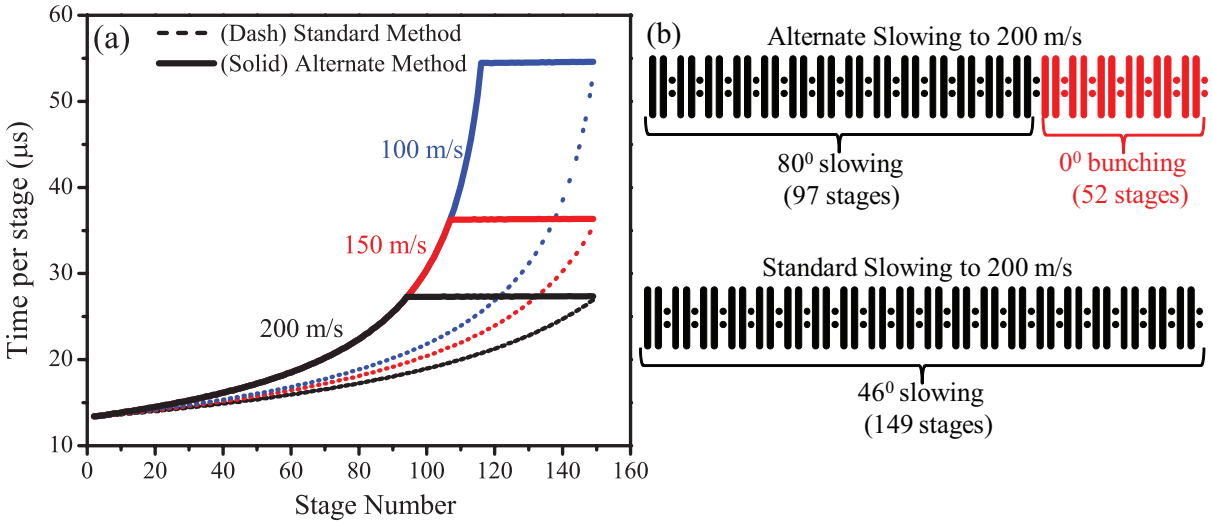

Figure 5.4: Deceleration schemes using both the standard and alternate methods. (a) The timing sequence to decelerate a packet of ND_3 molecules from 415 m/s to various velocities is shown with the time duration of each stage of deceleration plotted against the stage number. (b) A schematic representation of the two deceleration schemes decelerating from 415 m/s to 200 m/s. In the standard method of slowing, all 149 stages of the decelerator are used to decelerate the molecules at a constant 46° phase angle. In the alternate method of slowing, a high phase angle is chosen to aggressively slow the molecules using only the first 97 stages. The remaining stages are then operated at 0° phase angle to longitudinally and transversely guide the molecules to the interaction/detection region.

time is given by

$$\Delta t = \frac{(V_f - V_i)^2}{2V_f a_a} + \frac{L}{V_f} - \frac{V_f - V_i}{a_s}, \tag{5.1}$$

where V_i and V_f are the initial and final velocities of the packet, respectively, a_a and a_s are the accelerations of the synchronous molecule in the alternate and standard mode, and L is the length of the decelerator. This equation assumes a constant average acceleration during the slowing process that can be determined from the potential created by the electrodes [18].

Another advantage to operating in the alternate mode is the increase in energy resolution for collision experiments. For standard slowing, the velocity spread of the slowed packet increases for increasing velocity, as can be seen in figure 5.6. In addition to the large velocity spread, the distribution is far from Gaussian, as expected, leading to difficulty in characterizing the width for extracting parameters of collision measurements. The corresponding histograms for the alternate method are shown in red in figure 5.6(b). Here the velocity widths are considerably less, and the distributions are nearer to Gaussians. Because the initial phase-space acceptance is independent of final velocity, the velocity width for the alternate method remains almost constant as the velocity is changed (figure 5.7(a)). For our experimental parameters, we see a reduction in the velocity spread of up to a factor of ~ 5. It is useful to look at the improvement to the spread in terms of energy. The energy width of the packet as a function of final velocity for both methods is shown in figure 5.7(b). The decrease in energy spread of the molecular packet decelerated using the alternate method allows more precise determination of energy-dependent collisional cross-sections. However, this gain comes at a cost to molecular number and thus is not optimal for all types of experiments.

5.4 Phase-space rotation

Realizing a large decrease in energy spread of a molecular packet using our alternate method comes with one caveat. After the molecules are decelerated to the desired velocity, they are transported to the end of the decelerator under bunching conditions. While in the bunching stages,

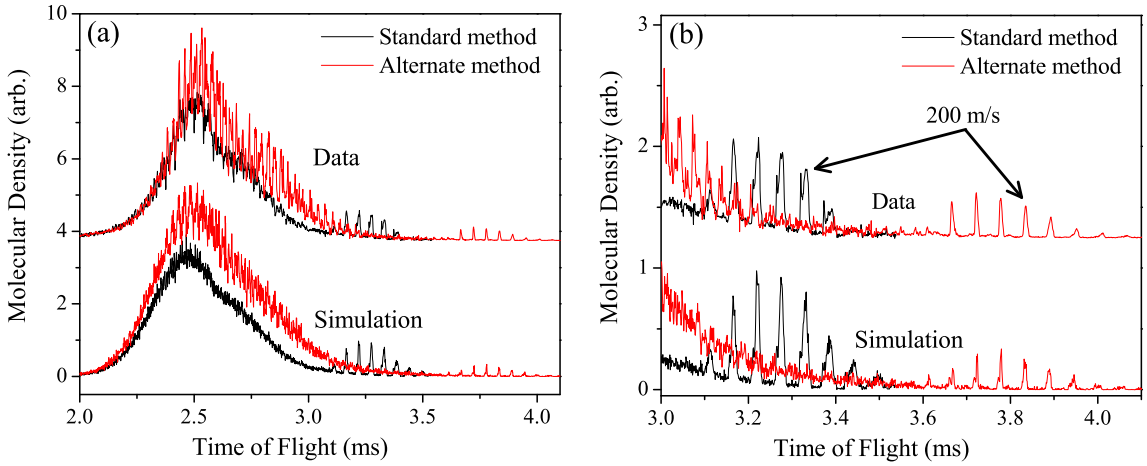

Figure 5.5: Time-of-flight traces comparing alternate and standard techniques. (a) Time-of-flight traces showing the arrival time of the decelerated peaks using both the standard and alternate methods of slowing. The traces shown are for a molecular beam that is decelerated from an initial speed of 415 m/s to a final speed of 200 m/s. Using the alternate deceleration method, the decelerated peak arrives 515 μs later than the analogous peak using the standard method. The data for both the standard and alternate methods are taken at 10 Hz, using a 15 mJ laser pulse focused with a 50 cm lens. Each point is averaged using 10 shots corresponding to a data acquisition of approximately one point/second. The results from a 3D Monte-Carlo simulation are also shown (lower curves). (b) Expanded time axis shown for clarity.

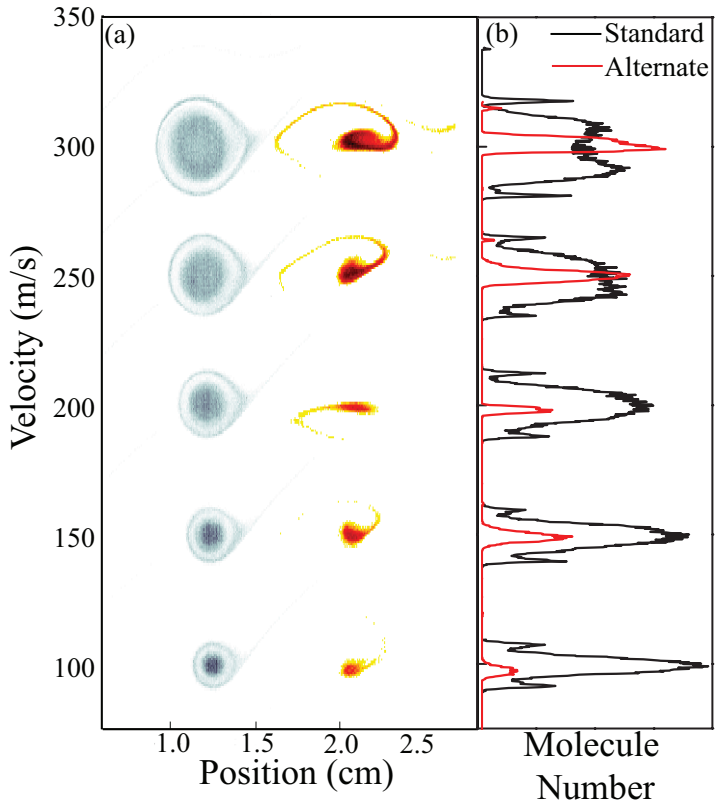

Figure 5.6: The (a) phase-space distributions at the end of the decelerator with (b) the corresponding velocity histograms. The distributions for the alternate method (red) are offset from the distributions for the standard method (blue) for clarity. The plots in (b) represent a histogram of velocities taken with a 1 × 1 mm horizontal cut through the molecular packet in the transverse direction.

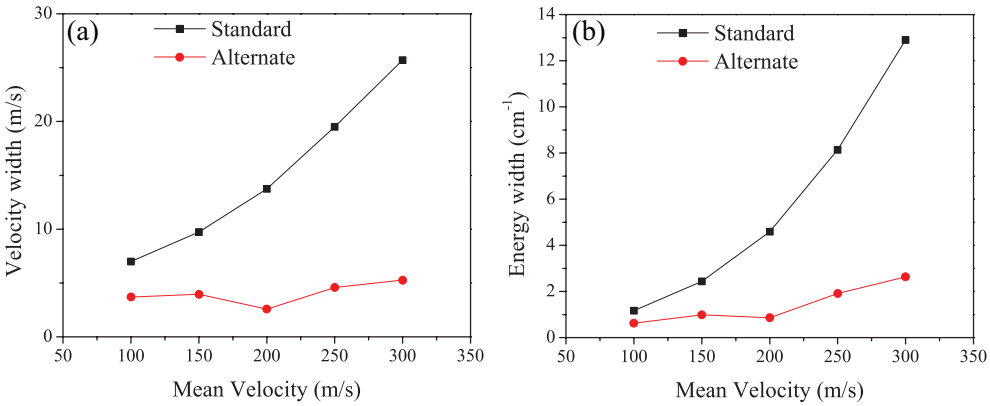

Figure 5.7: The (a) velocity widths and (b) corresponding energy widths of molecular packets for the standard and alternate deceleration methods. For standard slowing, there is a strong correlation between the phase angle (i.e., final velocity) and the energy width of the decelerated packet. In the alternate slowing method, however, the same phase angle is used for all final velocities. Therefore there is considerably less correlation, and the velocity width is effectively constant as a function of final velocity.

the molecular packet undergoes rotations in phase space. Through this rotation, the phase-space distribution will oscillate between having a wide velocity spread with a narrow position spread and having a narrow velocity spread with a wide position spread. Therefore it is critical to control this rotation such that the phase space has a narrow velocity spread at the detection/interaction region. We accomplish this phase rotation by varying the timing of the bunching in such a way as to change the rate of rotation without affecting the velocity of the packet. Phase-space rotation has also been demonstrated using additional electrodes with a different geometry [13] as well as using decelerator stages [52]. However, unlike in reference [52], we do not free-flight the molecules, but rather use a combination of bunching harmonics to efficiently transport the molecules to the end of the decelerator with the proper rotation.

Bunching can occur at harmonics of the fundamental bunching frequency while still maintaining phase stability [50]. First harmonic bunching occurs when the potential on the electrodes is switched every time the synchronous molecule crosses $\phi_0 = 0^\circ$ (i.e., directly between two electrode pairs). For third harmonic bunching, the potential is switched at every third stage. Bunching harmonics can be parameterized by a single parameter, S, which labels the harmonic order. The phase-space rotation frequency depends on the order of the bunching harmonic. The frequency of the rotation to first order is given by

$$\nu_s = \frac{\omega_z}{2\pi} = \sqrt{\frac{\Delta E}{4\pi S m l^2}}, \tag{5.2}$$

where ΔE is the maximum possible amount of Stark energy lost in a stage, m is the mass of the molecule, and l is the separation between the electrodes in the decelerator [50]. Under our experimental conditions, the frequency of rotation for $S = 1$ bunching is $\sim$1.4 kHz. Using both $S = 1$ and $S = 3$ bunching harmonics, we can manipulate the amount of rotation. The number of rotations the packet will undergo is given by

$$N_{rot} = \nu_1 t_1 \left[n_1 \left(1 - \frac{1}{\sqrt{3}} \right) + \frac{n_T}{\sqrt{3}} \right], \tag{5.3}$$

where t_1 is the time for an $S = 1$ bunching stage, n_1 is the number of $S = 1$ stages, and n_T is the total number of physical stages used for bunching. Figure 5.8 shows the rotation in phase space of a

packet decelerated to 200 m/s as it is bunched through the remainder of the slower. In this case, we use 37 $S = 1$ stages and 5 $S = 3$ stages, which results in a narrow velocity spread. The phase-space distribution undergoes just over 1.5 rotations and thus maintains the narrow velocity width created by our alternate slowing method. Figure 5.6 shows a tail of phase-stable molecules rotating around the packet in phase space. Although these molecules have a different velocity from the main packet, they contribute only a very small fraction to the total number of detected molecules, typically on the order of one percent.

There is a finite range of rotations accessible with a particular decelerator design and final velocity. The maximum number of rotations is achieved by using only $S = 1$ stages, and the minimum is achieved by using only $S = 3$ stages. This range is shown in figure 5.9. For most velocities, we can access any rotation angle.

In conclusion, we have developed a new protocol to run a Stark decelerator to achieve narrow energy spreads over a large range in velocities. We reduce the energy spreads by up to a factor of approximately five over traditional methods. These high-energy-resolution beams will enhance a variety of cold-molecule collision experiments using Stark decelerators.

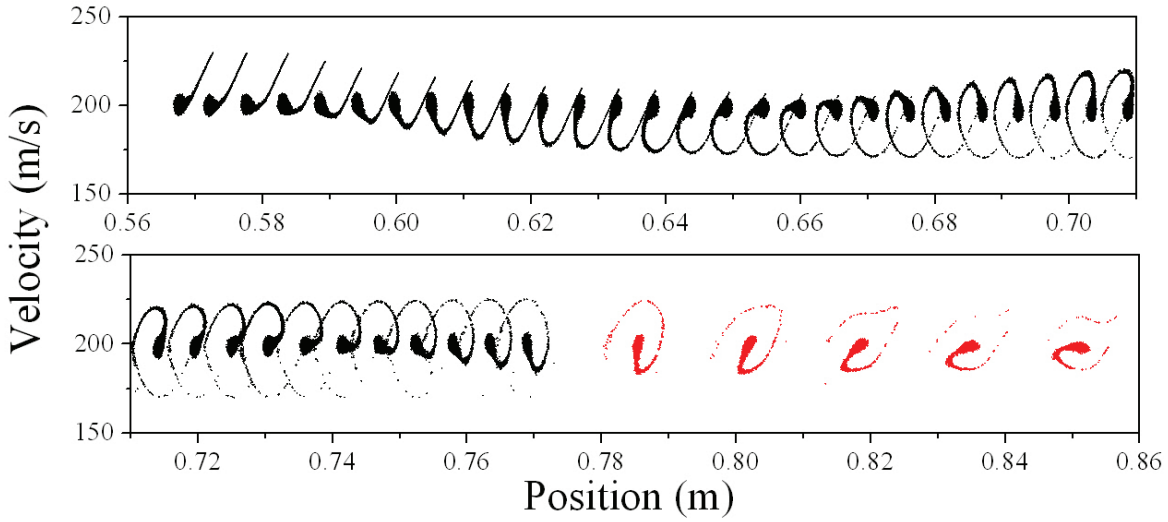

Figure 5.8: Phase-space rotations of the molecular packet during a bunching sequence. Each image is a snapshot of the phase-space distribution after a single bunching stage. The $S = 1$ stages are shown in black, and the $S = 3$ stages are in red. Oscillations in phase space of the packet during the bunching sequence leads to alternating broadening and narrowing of the velocity distribution as the packet traverses the remainder of the decelerator. The frequency of the oscillations can be manipulated (and hence the total number of oscillations) by an appropriate application of $S = 1$ and $S = 3$ bunching. In this example, the molecular packet is decelerated using the first 97 stages of the decelerator to 200 m/s. The desired rotation is achieved by 37 $S = 1$ bunching stages and 5 $S = 3$ stages.

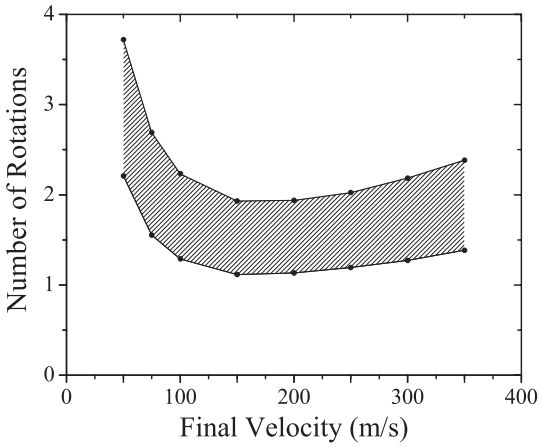

Figure 5.9: Calculated range over which the total number of rotations can be manipulated as a function of the final velocity for a decelerator of fixed length. The shaded region represents the accessible rotations.

Chapter 6

NH

While this thesis is about the interaction if Rb with ND_3 , when I started this work, I was actually attempting to decelerate the NH radical. I was unsuccessful in this attempt due to difficulties in the production of the free radical itself. However, with improved synthesis techniques and deceleration methods, future experiments with NH are likely to proceed. So presented here is a description of the Stark effect in NH.

6.1 Stark Effect in NH

NH is a free radical with a $X^3\Pi$ ground state and an $a^1\Delta$ metastable state. The $a^1\Delta$ experiences a Λ-doubling effect which is a result of the coupling between the nuclear rotation and the electronic angular momentum. This effect results in the splitting, E_Λ, of each state into opposite parity states, denoted f and e. The application of an electric field causes the two states to repel each other, giving rise the the Stark effect.

Because E_Λ for NH($a^1\Delta$) is only 115 kHz, it is reasonable to simplify the expression for the Stark effect to the purely linear case

$$W_{\text{Stark}} = \pm\mu|E|\frac{M_J\Omega}{J(J+1)}. \tag{6.1}$$

Where $\Omega = |\Lambda + \Sigma|$. Λ is the projection of L (the orbital angular momentum) onto the internuclear axis, and Σ is the projection of S (the spin angular momentum) onto the internuclear axis. This approximation works well for molecules with very small E_Λ, however, a more detailed analysis can

be made using the NH($a^1\Delta$) the Hamiltonian in the hyperfine basis. The Hamiltonian for the Stark effect is defined as

$$H_S = -\sum_q \mathcal{E}_q \left(D^1_{q0} \mu(\hat{\omega}) \right), \tag{6.2}$$

where, $\mathcal{E}_q$ is the electric field with projection q in the lab frame and D is the Wigner D-function. To construct the matrix, we work in the hyperfine basis [49]

$$|\Lambda J I_1 F_1 I_2 F M_F \pm\rangle = \frac{1}{\sqrt{2}}\{|\Lambda J I_1 F_1 I_2 F M_F\rangle \pm |-\Lambda J I_1 F_1 I_2 F M_F\rangle\}, \tag{6.3}$$

where Λ is the projection of L (the orbital angular momentum) onto the internuclear axis. I_1 is the nuclear spin of the nitrogen atom, I_2 is the nuclear spin of the hydrogen atom, $F = I_2 + F_1$, and $F_1 = I_1 + J$. The $\pm$ separating the first and second terms on the right-hand side specifies the parity (f/e) of the state. For this case we have,

$$\Lambda = \Omega = 2$$

$$J = 2$$

$$I_1 = 1$$

$$I_2 = 1/2$$

The hyperfine structure levels can then be calculated from the hyperfine Hamiltonian[1]

$$
\begin{aligned}
&\langle \alpha F \pm | H_{HF} | \alpha' F' \pm \rangle \\
&= \Lambda a_1 (-1)^{I_1+F_1+\Lambda} (2J+1) \sqrt{I_1(I_1+1)} I_1 \begin{pmatrix} J & 1 & j \\ -\Lambda & 0 & \Lambda \end{pmatrix} \begin{Bmatrix} F_1 & I_1 & J \\ 1 & J & I_1 \end{Bmatrix} \delta_{F_1,F_1'} \\
&+\Lambda a_2 (-1)^{I_2-I_1+F+\Lambda-1} (2J+1) \sqrt{I_2(I_2+1)(2I_2+1)(2F_1+1)(2F_1'+1)} \\
&\quad \times \begin{pmatrix} J & 1 & j \\ -\Lambda & 0 & \Lambda \end{pmatrix} \begin{Bmatrix} F_1 & F_1' & 1 \\ J & J & I_1 \end{Bmatrix} \begin{Bmatrix} F_1 & F_1' & 1 \\ I_2 & I_2 & F \end{Bmatrix} \delta_{F,F'} \\
&+(-1)^{I_1-F_1+\Lambda} (2J+1) \left(\frac{(2I_1+1)(2I_1+2)(2I_1+3)}{2I_1(2I_1-1)} \right)^{1/2} \begin{Bmatrix} I_1 & I_1 & 2 \\ J & J & F_1 \end{Bmatrix} \\
&\quad \times \left[\frac{eQq_1}{4} \begin{pmatrix} J & 2 & J \\ -\Lambda & 0 & \Lambda \end{pmatrix} \pm \frac{eQq_2}{4} \begin{pmatrix} J & 2 & J \\ -\Lambda & 2 & \Lambda \end{pmatrix} \delta_{\Lambda,1} \right] \delta_{F_1,F_1'},
\end{aligned}
\tag{6.4}
$$

where α is shorthand for all the quantum numbers in Eqn. 6.3 not listed in the bra-ket. α will be used in this manner throughout the rest of this analysis. The constants in the above equation are

$$a_1 = 110 \text{ MHz}$$

$$a_2 = 69.6 \text{ MHz}$$

$$eQq_1 = -8 \text{ MHz}$$

$$eqQ_2 = 0 \text{ MHz},$$

where eQq_1 and eQq_2 are the electric quadrupole constants for the nitrogen and a_1 and a_2 are the magnetic dipole interaction constants for the nitrogen and hydrogen respectively. The electric field mixes states of different F and F_1. The off-diagonal matrix elements are given by

$$\langle \alpha F \Omega \epsilon | D^1_{q\,0} | \alpha' F' \epsilon' \rangle = \frac{1}{2} \left(\langle \alpha F \Omega | \pm \langle \alpha F - \Omega | \right) D^1_{q\,0} \left(\alpha' F' \Omega' \rangle \pm | \alpha' F' - \Omega' \rangle \right). \tag{6.5}$$

We assume $\vec{\mathcal{E}} = \mathcal{E}\hat{e_z}$, which sets $q = 0$ in Eqn. 6.2. Then, through properties of the Wigner $3j$

[1] This hyperfine Hamiltonian for NH comes from Ubach, et. al. [49]. However the original paper does not have the $\delta_{F,F'}$ factor in the second term on the right hand side is missing. I assume this is an error as without the $\delta_{F,F'}$, the Hamiltonian is not Hermitian

symbol we have to two relations,

$$\begin{aligned}\langle \alpha F\Omega|D_0^1|\alpha F-\Omega\rangle &= 0\\ \langle \alpha F\Omega|D_0^1|\alpha F\Omega\rangle &= -\langle \alpha F-\Omega|D_0^1|\alpha F-\Omega\rangle,\end{aligned}$$

which leads to the constraint,

$$\langle \alpha e|D_0^1|\alpha e\rangle = \langle \alpha f|D_0^1|\alpha f\rangle = 0. \tag{6.6}$$

And thus, as we expect, only matrix elements mixing states of opposite parity survive. The surviving terms to be evaluated are

$$\begin{aligned}\frac{1}{2}\langle \alpha\Omega e|D_0^1|\alpha'\Omega' f\rangle &= \frac{1}{2}\langle \alpha\Omega f|D_0^1|\alpha'\Omega' e\rangle &(6.7)\\ &= \langle \alpha\Omega|D_0^1|\alpha\Omega\rangle, &(6.8)\end{aligned}$$

which, in terms of the reduced matrix elements of F becomes,

$$\langle \alpha F M_f|D_0^1|\alpha' F' M_f'\rangle = (-1)^{F-M_f}\begin{pmatrix} F' & 1 & F\\ m_f' & 0 & -m_f\end{pmatrix}\langle \alpha\|D_0^1\|\alpha' F'\rangle. \tag{6.9}$$

Recalling that $F = I_2 + F_1$ and $F_1 = I_1 + J$ and further reducing the matrix elements using Wigner $3j$ and $6j$ symbols gives

$$\begin{aligned}\langle \alpha F(I_2,F_1)\|D_0^1\|\alpha' F'(I_2'F_1')\rangle &= (-1)^{1+I_2+F_1+F}[F,F']\begin{Bmatrix} F_1 & F & I_2\\ F' & F_1' & 1\end{Bmatrix} &(6.10)\\ &\quad\times\langle \alpha F_1(I_1,J)\|D_0^1\|\alpha' F_1'(I_1'J')\rangle\\ \langle \alpha F_1(I_1,J)\|D_0^1\|\alpha' F_1'(I_1'J')\rangle &= (-1)^{1+F_1+I_1+J}[F_1,F_1']\begin{Bmatrix} J & F_1 & I_1\\ F_1' & J' & 1\end{Bmatrix} &(6.11)\\ &\quad\times\langle \alpha J\|D_0^1\|\alpha' J'\rangle\\ \langle \alpha J\|D_0^1\|\alpha' J'\rangle &= (-1)^{J-\Omega}\begin{pmatrix} J & 1 & J'\\ -\Omega & 0 & \Omega\end{pmatrix}(2J+1), &(6.12)\end{aligned}$$

where the notation $[X_1, X_2, \cdots]$ is shorthand for $\sqrt{(2X_1+1)(2X_2+1)\cdots}$. Putting all the above

terms together gives the final result,

$$\begin{aligned}\langle\alpha|H_S|\alpha'\rangle &= -\mu\mathcal{E}[J,F,F',F_i,F_1'](-1)^{(F'-M)+(1+I_2+F_1+F)+(1+I_1+J+F_1)+(J-\Omega)} \\ &\times \begin{pmatrix} J & 1 & J' \\ -\Omega & 0 & \Omega \end{pmatrix} \begin{pmatrix} F' & 1 & F \\ m_f' & 0 & -m_f \end{pmatrix} \\ &\times \begin{Bmatrix} F_1 & F & I_2 \\ F' & F_1' & 1 \end{Bmatrix} \begin{Bmatrix} J & F_1 & I_1 \\ F_1' & J' & 1 \end{Bmatrix}\end{aligned} \tag{6.13}$$

Figure 6.1 and 6.2 show the Stark effect for NH($a^1\Delta$) in the high- as well and low-field limit, respectively. From Figure 6.2 it is clear that the Stark shift becomes linear almost immediately and therefore the linear approximation given in Eqn. 6.1 is adequate.

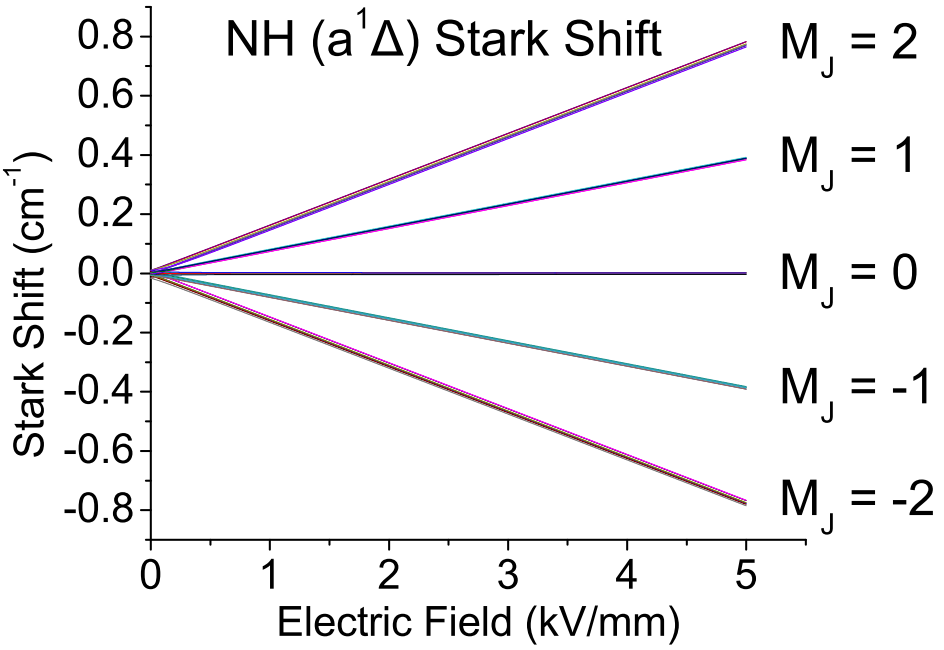

Figure 6.1: NH Stark Shift.

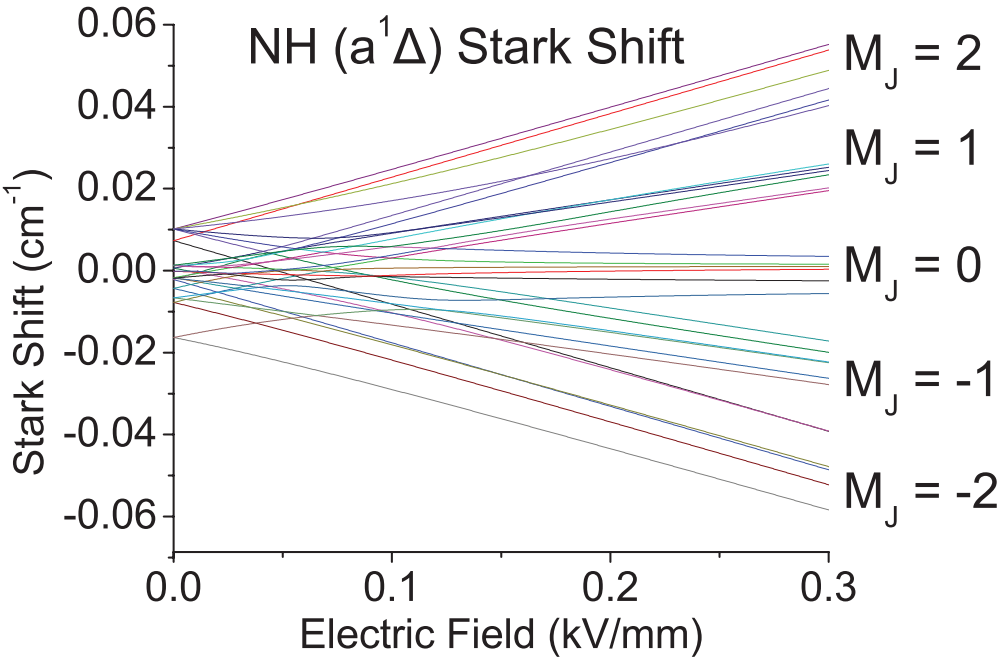

Figure 6.2: NH Stark Shift at low field.

Bibliography

[1] M.N.R. Ashfold and J.D. Howe. Multiphoton spectroscopy of molecular species. Ann. Rev. Phys. Chem, 45:57–82, 1994.

[2] M.N.R. Ashfold, S.R. Langford, R.A. Morgan, A.J. Orr-Ewing, C.M. Western, C.R. Scheper, and C.A. de Lange. Resonance enhanced multiphoton ionization (rempi) and rempi-photoelectron spectroscopy of ammonia. The European Physical Journal D - Atomic, Molecular, Optical and Plasma Physics, 4:189–197, 1998. 10.1007/s100530050199.

[3] P. F. Barker and M. N. Shneider. Slowing molecules by optical microlinear deceleration. Phys. Rev. A, 66(6):065402, Dec 2002.

[4] H. L. Bethlem, A. J. A. van Roi, R. T. Jongma, and G. Meijer. Alternate gradient focusing and deceleration of a molecular beam. Phys. Rev. Lett., 88:133003, 2002.

[5] H. L. Bethlem, M. R. Tarbutt, J. Küpper, D. Carty, K. Wohlfart, E. A. Hinds, and G. Meijer. Alternate gradient focusing and deceleration of polar molecules. J. Phys. B, 39:R263–R291, 2006.

[6] Hendrick L. Bethlem, Giel Berden, and Gerard Meijer. Decelerating neutral dipolar molecules. Phys. Rev. Lett., 83:1558–1561, 1999.

[7] Hendrick L. Bethlem, Floris M. H. Crompvoets, Rienk T. Jongma, Sebastiaan Y.T. van de Meerakker, and Gerard Meijer. Deceleration and trapping of ammonia using time-varying electric fields. Phys. Rev. A, 65:053416, 2002.

[8] Hendrick L. Bethlem, Jacqueline van Veldhoven, Melanie Schnell, and Gerard Meijer. Trapping polar molecules in an ac trap. Phys. Rev. A, 74(6):063403, Dec 2006.

[9] J. R. Bochinski, Eric R. Hudson, H. J. Lewandowski, Gerard Meijer, and Jun Ye. Phase space manipulation of cold free radical OH molecules. Phys. Rev. Lett., 91:243001, 2003.

[10] O. Bucicov, M. Nowak, Jung S., G. Meijer, and E. Tiemann. Cold SO_2 molecules by stark deceleration. The European Physical Journal D, 43:463–469, 2008.

[11] Comsol. www.comsol.com.

[12] Glen Cowen. Statistical Data Analysis. Oxford University Press, New York, 1998.

[13] Floris M. H. Crompvoets, Rienk T. Jongma, Hendrick L. Bethlem, André J. A. van Roij, and Gerard Meijer. Longitudinal focusing and cooling of a molecular beam. Phys. Rev. Lett., 89(9):093004, Aug 2002.

[14] David Fogel. Evolutionary Compuation, 2nd Ed. IEEE Press, Piscataway, NJ, 2000.

[15] J. J. Gilijamse, S. Hoekstra, N. Vanhaecke, S. Y. T. van de Meerakker, and G. Meijer. Loading Stark-decelerated molecules into electrostatic quadrupole traps. European Physical Journal D, 57:33–41, March 2010.

[16] Joop J. Gilijamse, Steven Hoekstra, Sebastiaan Y. T. van de Meerakker, Gerrit C. Groenenboom, and Gerard Meijer. Near-Threshold Inelastic Collisions Using Molecular Beams with a Tunable Velocity. Science, 313(5793):1617–1620, 2006.

[17] Joop J. Gilijamse, Steven Hoekstra, Sebastion Y. T. van de Meerakker, Gerrit C. Goenenboom, and Gerard Meijer. Near-threshold inelastic collisions using molecular beams with a tunable velocity. Science, 313:1617–1618, 2006.

[18] Koos Gubbels, Gerard Meijer, and Bretislav Friedrich. Analytic wave model of stark deceleration. Phys. Rev. A, 73:063406–+, 2006.

[19] Gregory Hall, Kopin Liu, Michael J. McAuliffe, Clayton F. Giese, and W. Ronald Gentry. Pulsed molecular beam study of state-to-state vibrational excitation in He+I_2 collisions: Energy dependence of the v=0→1 cross section. J. Chem. Phys., 78:5260–5261, 1983.

[20] Gerhard Herzberg. Molecular Spectra and Molecular Structure. II Infrared and Raman Spectrra of Polyatomic Molecules. Krieger Publishing Company, reprint edition (1991) edition, 1945.

[21] http://nobelprize.org/nobelprizes/chemistry/laureates/1986/. "the nobel prize in chemistry 1986".

[22] Eric R. Hudson, Christopher Ticknor, Brian C. Sawyer, Craig A. Taatjes, H.J. Lewandowski, J.R. Bochinski, J.L. Bohn, and Jun Ye. Production of cold formaldehyde molecules for study and control of chemical reaction dynamics with hydroxyl radicals. Phys. Rev. A, 73:063404–+, 2006.

[23] Piotr S. Żuchowski and Jeremy M. Hutson. Prospects for producing ultracold nh_3 molecules by sympathetic cooling: A survey of interaction potentials. Phys. Rev. A, 78(2):022701, Aug 2008.

[24] Piotr S. Żuchowski and Jeremy M. Hutson. Low-energy collisions of nh_3 and nd_3 with ultracold rb atoms. Phys. Rev. A, 79(6):062708, Jun 2009.

[25] R. M. Jordan. http://www.rmjordan.com/c211-451.html.

[26] V. Roman Krems, C. William Stwalley, and Bretislav Friedrich. Cold Molecules: Theory, Experiment, Applications. CRC Press, 2009.

[27] C. Krenn, W. Scherf, O. Khait, M. Musso, and L. Windholz. Stark effect investigations of resonance lines of neutral potassium, rubidium, europium and gallium. Zeitschrift fr Physik D Atoms, Molecules and Clusters, 41:229–233, 1997. 10.1007/s004600050315.

[28] Manuel Lara, John L. Bohn, Daniel E. Potter, Pavel Soldán, and Jeremy M. Hutson. Cold collisions between OH and Rb: The field-free case. Phys. Rev. A, 75:012704, 2007.

[29] R. D. Levine and Bernstein R. B. Molecular Reaction Dynamics and Chemical Reactivity. Oxford University Press, New York, 1987.

[30] R. Locht. The photoionization of ammonia revisited. The vibrational autoionization of NH3 and its three isotopomers in the 10 12 eV photon energy range. Chemical Physics, 155:407–422, September 1991.

[31] R. G. Macdonald and L. Kopin. State-to-state integral cross sections for the inelastic scattering of CH($X^2\Pi$)+He: Rotational rainbow and orbital alignment. J. Chem. Phys., 91:821, 1989.

[32] L. Machin and E. Roueff. Rotational excitation and de-excitation of interstellar ammonia in collisions with helium. Journal of Physics B Atomic Molecular Physics, 38:1519–1534, May 2005.

[33] Harold J. Metcalf and Peter van der Straten. Laser Cooling and Trapping. Springer-Verlag, New York, 1999.

[34] E. Narevicius, C. G. Parthey, A. Libson, J. Narevicius, I. Chavez, U. Even, and M. G. Raizen. An atomic coilgun: using pulsed magnetic fields to slow a supersonic beam. New Journal of Physics, 9:358–+, October 2007.

[35] I. P. Omelyan, I. M. Myrglod, and R. Folk. Optimized forestruth- and suzuki-like algorithms for integration of motion in many-body systems. Computer Physics Communications, 146:188–202, 2002.

[36] L P Parazzoli, N Fitch, D S Lobser, and H J Lewandowski. High-energy-resolution molecular beams for cold collision studies. New Journal of Physics, 11(5):055031, 2009.

[37] A. Picard-Bersellini, H. Aroui, M. Broquier, and S. Blanchard. Collision cross sections between some rovibrational states of ammonia gas perturbed by hydrogen. International Journal of Infrared and Millimeter Waves, 10:251–255, 1989. 10.1007/BF01011240.

[38] Juan Pino. Private communications.

[39] D. Proch and T. Trickl. A high-intensity multi-purpose piezoelectric pulsed molecular beam source. Review of Scientific Instruments, 60:713–716, April 1989.

[40] B. C. Sawyer, B. K. Stuhl, B. L. Lev, J. Ye, and E. R. Hudson. Mitigation of loss within a molecular Stark decelerator. European Physical Journal D, 48:197–209, July 2008.

[41] B. C. Sawyer, B. K. Stuhl, M. Yeo, T. V. Tscherbul, M. T. Hummon, Y. Xia, J. Klos, D. Patterson, J. M. Doyle, and J. Ye. Cold heteromolecular dipolar collisions. ArXiv e-prints, August 2010.

[42] Brian C. Sawyer, Bennjamin K. Stuhl, Dajun Wang, Mark Yeo, and Ye Jun. Molecular beam collisions with a magnetically trapped target. Phys. Rev. Lett., 101:203203, 2008.

[43] Ludwig Scharfenberg, Henrik Haak, Gerard Meijer, and Sebastiaan Y.T. van de Meerakker. Operation of a stark decelerator with optimum acceptance, 2008.

[44] Giacinto Scoles. Atomic and Molecular Beam Methods. Oxford University Press, New York, 1988.

[45] Rex T. Skodje, Dimitris Skouteris, David E. Manolopoulos, Shih-Huang Lee, Feng Dong, and Kopin Liu. Resonance-mediated chemical reaction: $f + hd \rightarrow hf + d$. Phys. Rev. Lett., 85(6):1206–1209, Aug 2000.

[46] D. M. Sonnenfroh, R. G. MacDonald, and K. Liu. A crossed-beam study of the state-resolved integral cross sections for the inelastic scattering of OH(X II-2) with CO and N_2. J. Chem. Phys., 94:6508–6518, May 1991.

[47] Daniel Steck. The angular distribution of resonance fluorescence from a zeeman-degenerate atom: Formalism. Unpublished, available on-line at http://www.ph.utexas.edu/ quantopt.

[48] M. R. Tarbutt, H. L. Bethlem, J. J. Hudson, V. L. Ryabov, V. A. Ryzhov, B. E. Sauer, G. Meijer, and E. A. Hinds. Slowing heavy, ground-state molecules using an alternating gradient decelerator. Phys. Rev. Lett., 92(17):173002–+, 2004.

[49] W. Ubachs, G. Meyer, J. J. ter Meulen, and A. Dymanus. High-resolution spectroscopy on the c1[pi] ¡– a1[delta] transition in nh. Journal of Molecular Spectroscopy, 115(1):88 – 104, 1986.

[50] Sebastiiaan Y. T. van de Meerakker, Nicolas Vanhaecke, Hendrick L. Bethlem, and Gerard Meijer. Higher-order resonances in a stark decelerator. Phys. Rev. A, 71:053409–+, 2005.

[51] Jacqueline van Veldhoven, Hendrick L. Bethlem, Melanie Schnell, and Gerard Meijer. Versatile electrostatic trap. Phys. Rev. A, 73(6):063408, Jun 2006.

[52] J. van Veldhoven, J. Küpper, H. L. Bethlem, B. Sartakov, A. J. A. van Roij, and G. Meijer. Decelerated molecular beams for high-resolution spectroscopy. Eur. Phys. J. D, 31:337–349, 2004.

[53] Jacquiline Veldhoven. AC Trapping and High-Resolution Spectroscopy of Ammonia Molecules. PhD thesis, Vrije Universiteit, Amsterdam, 2006.

[54] H. Wallis, J. Werner, and W. Ertmer. Magneto-optical trapping of atoms. At. Mol. Phys., 28:275–300, 1993.

[55] Carl Wieman, Gwenn Flowers, and Sarah Gilbert. Inexpensive laser cooling and trapping experiment for undergraduate laboratories. American Journal of Physics, 63(4):317–330, 1995.

[56] W. C. Wiley and I. H. McLaren. Time-of-flight mass spectrometer with improved resolution. Rev. Sci. Instrum., 26:1150–1157, 1955.

[57] K. Wohlfart, F. Filsinger, F. Gratz, J. Kupper, and G. Meijer. Stark deceleration of oh radicals in low-field-seeking and high-field-seeking quantum states. Phys. Rev. A, 78:033421, 2008.